Designing and Testing the Neutron Source Deployment System and Calibration Plan for a Dark Matter Detector

by

Shawn Westerdale

Submitted to the Department of Physics
in partial fulfillment of the requirements for the degree of

Bachelor of Science in Physics

at the

MASSACHUSETTS INSTITUTE OF TECHNOLOGY

June 2010
[JUNE 2011]

Author ....
Department of Physics
May 6, 2010

Certified by. ....
Jocelyn Monroe
Assistant Professor
Thesis Supervisor

Accepted by.... ....
Professor Nergis Mavalvala
Senior Thesis Coordinator, Department of Physics

Designing and Testing the Neutron Source Deployment System and Calibration Plan for a Dark Matter Detector

by

Shawn Westerdale

Submitted to the Department of Physics
on May 6, 2010, in partial fulfillment of the
requirements for the degree of
Bachelor of Science in Physics

Abstract

In this thesis, we designed and tested a calibration and deployment system for the MiniCLEAN dark matter detector. The deployment system uses a computer controlled winch to lower a canister containing a neutron source into the detector where the neutron source pulses to produce calibration data. The winch then pulls the neutron source back out of the detector. We found that the deployment system position is precise to under 0.05 cm, one tenth of the minimum required precision. We designed a canister that will hold the neutron source during the calibration process. The canister will contain a dielectric gel to thermally and electrically insulate the high voltage electronics and the neutron source from the rest of the detector. We calculated the equilibrium temperature change of the calibration neutron source when it is turned on and found that the temperature increases by $92.6^{+56.8}_{-18.8}$ K, corresponding to a rise in the dielectric gel height of $1.50^{+0.96}_{-0.32}$ cm. This temperature change is within the service temperature range of the dielectric gel; however, a more thermally conductive gel could still be used to reduce the temperature increase. We simulate the background external neutrons in MiniCLEAN and find that the addition of an air-filled calibration tube to the basic MiniCLEAN design has little effect on the external neutron background rate. Lastly, we simulate the calibration process in order to determine how long we must calibrate MiniCLEAN in order to obtain the desired 5% statistical precision on measurements of the calibration neutron-induced recoil spectrum. We found that a minimum of 2.48×10^6 neutrons are needed to measure the total counts in the region of interest in energy to 5% (corresponding to a pulse mode calibration time of 124 seconds assuming that neutrons are produced at a rate of 10^5 per second), and 2.02×10^7 neutrons are needed to achieve 5% measurements of the energy spectrum with 2 KeVee binning in the region of interest (corresponding to a time of 1005 seconds).

Thesis Supervisor: Jocelyn Monroe
Title: Assistant Professor

Acknowledgments

First and foremost, I would like to thank my advisor Professor Jocelyn Monroe for putting up with me for most of these last four years and being a great mentor to me as I developed as a physicist. I don't think I can express my gratitude for all that she has done to help me learn the ins and outs of being a physicist and for helping me set the course for the next step in my career, in addition to all that she has done to help me produce this thesis.

I would also like to thank Kim Palladino for patiently answering my questions whenever I got confused. Your guidance and support were incredibly instrumental in doing all of the research and analysis that went into writing this document. I also want to express my gratitude to Lu Feng and the entire MIT MiniCLEAN group for working with me as I progressed through my research and for helping me figure things out whenever I got stuck on a problem.

I would also like to extend a warm thank you out to the Weak Interactions Team at Los Alamos National Laboratory. I am especially grateful to Vince Guiseppe for being both a mentor and a friend as I was working some place new somewhere far from home. I am also indebted to Keith Rielage and Andrew Hime for accepting me onto their team and helping me learn what it is like to be a physicist.

While at MIT, I have taken many great classes with many amazing professors. One professor who particularly stands out, though, is Professor Janet Conrad, my particle physics professor. Your friendly guidance and brilliant instruction has helped inspire me to pursue particle physics and have stuck with me as a constant reminder of how much fun one can have while exploring the inner workings of the universe. I would also like to thank Professor Nergis Mavalvala, my Junior Lab instructor, who helped make one of my most stressful terms at MIT also one of my most fun and educational terms. Many of the data collection and analysis techniques that went into producing this thesis I learned from you.

Contents

List of Figures

List of Tables

Chapter 1

Introduction

Luminous matter, the matter that we see and interact with on a daily basis can be accurately detected in outer space and measured using astrophysical techniques. However, it has been observed through evidence discussed in Section 1.1 that many bodies in the universe behave as if they have more mass than can be observed with the aforementioned techniques. This mass difference is accounted for by models that include dark matter. Dark matter is matter that demonstrates gravitational effects but cannot be detected via electromagnetic interactions. Despite the difficulty of detecting it, current estimates of the dark matter distribution in the universe claim that 83% of the matter density of the universe is made up of dark matter [18], making it far more abundant than any other form of matter that we know of.

The two leading dark matter candidates are WIMPs and axions, discussed in Section 1.2. While it is possible that both of these models are correct and that the dark matter we observe is some mixture of these proposed particles, to determine the nature of dark matter we must first detect it. Then we can begin narrowing models down and determining the mass of different types of dark matter particles so that these previously unobservable forms of matter can finally be understood.

While there are many different experiments currently being developed to search for each of these forms of dark matter, discussed in Section 1.3, this thesis focuses on MiniCLEAN, a dark matter detector searching for WIMPs with masses between 10 and 100 GeV/c^2. MiniCLEAN is discussed in Section 1.4. Before MiniCLEAN can begin operation, it is important that it be well calibrated in order to achieve the required precision—especially because the probability of a WIMP interactions is so low that it is important to measure whatever events are detected as precisely as possible.

The primary focus of this thesis is the neutron calibration system for MiniCLEAN. Chapter 3.2 discusses the canister that will hold the calibration neutron source, and the source is described in Chapter 3.1. In Chapter 2 we discuss the deployment system; its accuracy and precision at lowering the canister to a specified depth is then discussed in Chapter 2.6. We will then discuss in Chapter 4 simulations of the calibration made in GEANT4 in order to determine how long we must calibrate the detector in order achieve this desired precision.

1.1 Evidence for Dark Matter

Three observations that have necessitated the existence of dark matter come from measurements taken from rotational velocities around spiral galaxies, measurements of the gravitational lensing around the bullet cluster, and measurements taken by the WMAP experiment of the Cosmic Microwave Background. The first observation is that the rotational velocities of spiral galaxy arms do not decrease with distance from the center of the galaxy as the visible luminous matter would predict. This observation is discussed in greater detail in Section 1.1.1. The second observation is that the center of visible mass of the bullet cluster, a pair of colliding galaxy clusters, does not agree with the center of gravitational lensing; this observation is further discussed in Section 1.1.2. The third observation is that the total mass of baryonic and leptonic matter in the universe does not account for the total matter density measured by WMAP; this observation is discussed in Section 1.1.3.

1.1.1 Galactic Rotation Curve

The first definitive evidence for dark matter came from measurements of galactic rotation curves taken by Louise Volders in 1959.

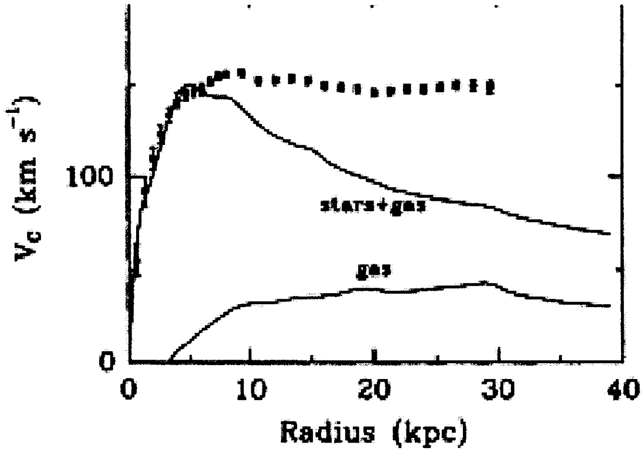

Figure 1-1: The measured galactic rotation velocity (in km/s) versus the distance from the center of the galaxy (in kpc) for the NGC 1398 galaxy. The dotted points show the measured velocities and the lines show the gaseous and stellar contributions to this velocity, as labeled. The difference between these two velocity distributions indicates the presence of matter that is not accounted for by the galactic model or that gravity does not behave as expected [3].

Galaxies typically consist of a dense inner sphere of stars around a central black hole and a sparse disk of stars that reach far out from the center of the galaxy. The vast majority of the observable matter in the galaxy appears within the dense inner ball, and so without accounting for dark matter, we can predict how fast the galaxy should be spinning at a distance r from the center by assuming that the entire mass of the galaxy is located in this region. This analysis concludes that within the central ball, the measured orbital velocities should increase linearly with r. Outside this region, the velocities are predicted to drop off as $\frac{1}{\sqrt{r}}$. The total gaseous and stellar contributions to the galactic rotation curve in figure 1-1 shows this expected velocity distribution.

These velocities can be directly measured with the 21cm wavelength line emitted by spin-flip transitions within hydrogen. Since most of the galaxy is made of hydrogen, this line can be used to consistently measure the velocity at any distance from the center of the galaxy by considering how much the signal that reaches the earth has been Doppler shifted. Plotting the resulting velocity curve yields the dotted curve in figure 1-1. This curve agrees with the prediction within the central ball, but then differs drastically from the prediction in the sparse region.

This difference is an indication that the model neglecting dark matter and assuming Newtonian gravity is wrong and therefore lends strong evidence supporting the dominance of dark matter within the galaxy [43]. Assuming a spherically symmetric dark matter halo, de Blok and McGaugh have shown that the observed rotation curve can be explained by a dark matter density distribution given by

$$\rho(r) = \rho_0 \left[1 + \left(\frac{r}{R_c}\right)^2\right]^{-1} \tag{1.1}$$

where ρ_0 is the central density of the halo and R_c is the core radius of the halo [43]. Figure 1-2 shows the measured galactic rotation curve of the NGC 1560 galaxy with the maximal contributions to the rotation curve from gas, the stellar disk, and the dark halo. The latter uses the density given by equation 1.1 and predicts that $\rho_0 = 5.9 \times 10^{-3}$ solar masses per parsec and that $R_c = 6.2$ kpc [11].

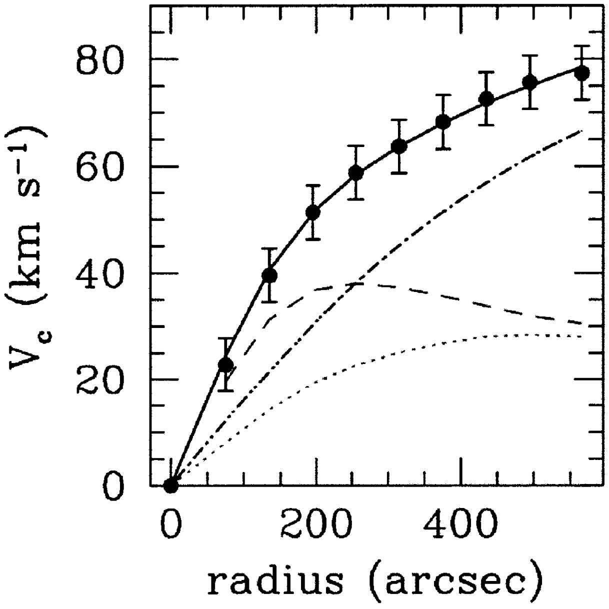

Figure 1-2: Rotation velocity (in km/s) versus distance from center of galaxy (in arcsec). Measured galactic rotation curves of NGC 1560 fit with maximum contributions from the gas component (dotted line), from the stellar disk (dashed line), and from the dark halo (dash-dotted line). [11]

1.1.2 Bullet Cluster

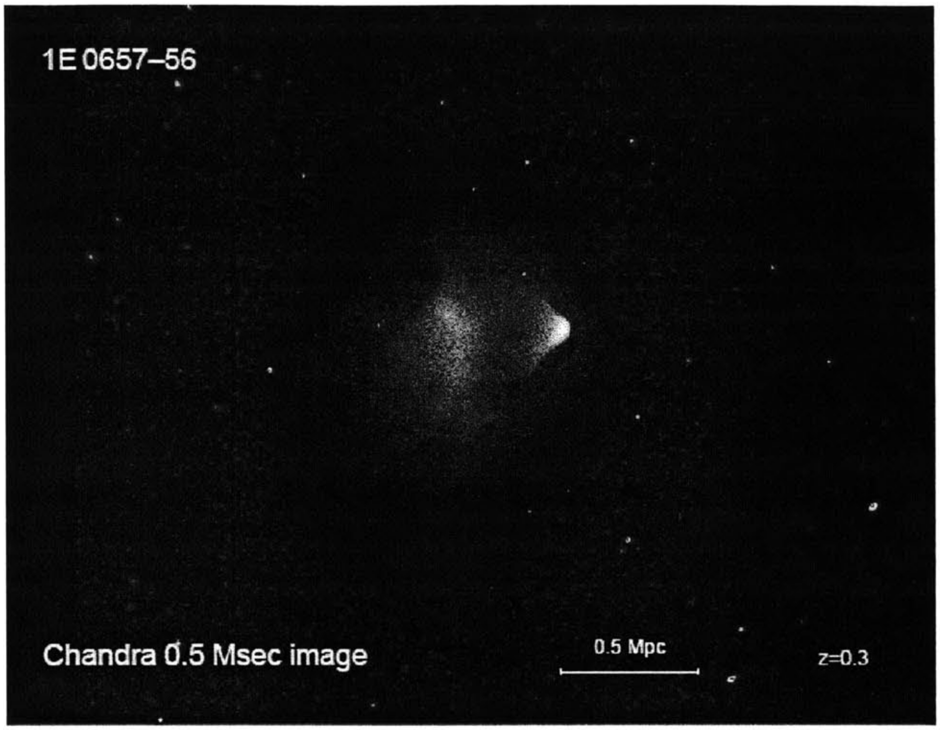

Figure 1-3: An x-ray photograph of the bullet cluster, taken by the Chandra X-Ray Observatory [38].

The bullet cluster, consisting of two clusters of galaxies that have collided, provides a key piece of evidence suggesting that dark matter rather than a modified theory of gravity is cause of the missing mass discussed in Section 1.1.1. Standard galactic models divide the matter in galaxies into three types: stars, gas, and dark matter (other bodies such as planets are sufficiently small that their masses can be neglected). Of the two forms of luminous matter, the gas has significantly more mass than the stars, and so we can effectively track the dynamics of a galaxy by only observing the gas, which is observable by x-ray emissions. Figure 1-3 shows the x-ray measurements of the gases of the two galaxies interacting as they collide and subsequently slow down as they pass through each other [14]. From these images, the center of mass of both galaxies can be determined, considering only the mass that comes from the gas.

The mass of the galaxies can also be determined by measuring gravitational lensing around and through the cluster. Large bodies can have sufficiently strong gravitational fields to bend light significant distances. When this happens, objects that appear behind or near the large body in the night sky may appear to be displaced. This effect is known as gravitational lensing. By measuring the deflection of light around an object, the mass of that object can therefore be determined. When this analysis is applied to the bullet cluster in order to measure its center of mass, the result differs from the center of mass measured by the x-ray image by eight standard deviations. This difference definitively shows that the visible mass cannot account for all of the mass of the clusters, and that an alteration of the gravitational force law cannot explain the observations, necessitating the existence of dark matter. [14]

1.1.3 WMAP

The Wilkinson Microwave Anisotropy Probe (WMAP) measures differences in the Cosmic Microwave Background temperature across the sky; by measuring the slight variations in this background, WMAP can determine the density of dark matter in the universe. WMAP measures many parameters relevant to the ΛCDM model of the universe—the leading cosmological model, including dark energy and dark matter. From the temperature fluctuations, WMAP determines the current composition of the universe through analysis of the power spectrum of the two-point correlation function. After running for five years, WMAP was able to rule out the possibility of a dominantly hot dark matter model (a model in which dark matter consists of light, relativistic particles) and determine the relative abundances of different forms of matter in the universe. WMAP measured the baryonic closure fraction of the universe—the minimum fraction of the total energy density of the universe required for the universe to be closed—to be $\Omega_b = 0.0456 \pm 0.0015$, the cold dark matter closure fraction to be $\Omega_c = 0.228 \pm 0.013$, and the dark energy closure fraction to be $\Omega_\Lambda = 0.726 \pm 0.015$ [18]. The matter content of the universe as measured by WMAP today is shown in figure 1-4.

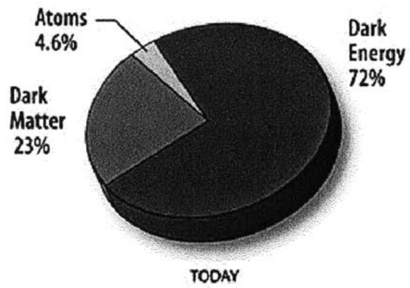

Figure 1-4: The energy density of dark energy, atoms, and dark matter, measured by WMAP [46].

1.2 Dark Matter Particle Candidates

Despite its abundance, the nature of dark matter particles, other than that they have gravitational interactions, is unknown. However, many models of dark matter based on physical observations and possible extensions to the Standard Model can potentially explain observations. The leading models are currently WIMPs and axions, discussed below. This section will also discuss MaCHOs and sterile neutrinos, which are models that may be able to account for part of the observed abundance but not all of it.

1.2.1 WIMPs

WIMPs, or Weakly Interacting Massive Particles, are theoretical particles that interact only via gravitational and weak forces. Since these particles do not interact with electromagnetic fields, they cannot be detected through standard optical means. If WIMPs do interact via the weak force, then they would be detectable through nuclear recoils within a target medium. The interaction cross section scale is 10^{-44} cm^2, and therefore WIMP detectors must have very low background and high precision.

While WIMPs are similar to neutrinos in that they interact only through the gravitational and weak forces, they are predicted to have much higher masses (on the GeV/c^2 scale), and therefore move much more slowly. For this reason, WIMPs constitute cold dark matter, i.e. slowly-moving dark matter that forms clumps. Simulations of the evolution of a universe containing only cold dark matter result in clumps of dark matter that have size and density distributions that agree with those observed in the universe[5]. Such simulations limit hot dark matter, relativistic dark matter, to contributing no more than 10% of the total observed dark matter.

In addition to being a cold dark matter candidate, WIMPs are predicted by most models of supersymmetry. The Standard Model in its currently accepted form does not predict any particles that have the properties that are expected of WIMPs. However, all supersymmetric extensions to the Standard Model require a lightest supersymmetric particle (LSP), which by conservation of R-parity[1] must be stable. Additionally, most supersymmetric models require that the LSP have a mass on the GeV to TeV scale, be weakly interacting, and not interact with the strong or electromagnetic force, and so the LSP must be a WIMP. Various supersymmetric models predict that WIMPs be either neutralinos, gravitinos, sneutrinos, or a superposition of these [28]. Since WIMPs are predicted by supersymmetry and would constitute cold dark matter, they are one of the favored candidates for dark matter.

1.2.2 Axions

The other favored candidate for dark matter is the axion, which is a theoretical particle postulated in order to solve the strong CP problem in the Standard Model. Among the symmetries observed in particle physics, there are charge conjugation, parity, and time symmetries, abbreviated as C,P, and T. C symmetry means that interchanging every particle in a system with its antiparticle would have no observable effect. Similarly, a system that exhibits P symmetry is left unchanged if all of the coordinates change sign, and a system that has T symmetry remains the same if time were to flow in reverse.

Experiments have consistently shown that the strong force and quantum chromodynamics obey the combination of C and P symmetries, CP. However, the Standard Model does not provide any explanation for why this is so; in fact, it predicts that there should be some probability that a QCD interaction violate CP symmetry. The

---

[1] R-parity is a symmetry expressed in supersymmetric models that forbids supersymmetric particles from becoming Standard Model and vice versa

fact that this CP violation is never observed is known as the strong CP problem, and the axion is a particle that is introduced by Peccei-Quinn theory to solve this problem. The axion carries a field that cancels with the parameter that makes the Standard Model predict CP violation, making the probability of a QCD interaction violating CP symmetry effectively zero [41].

Axions are predicted to have no electric charge and to primarily interact with fermions by converting into two photons with a coupling constant given by $g_{a\gamma\gamma} = (1.1 \times 10^{-34}\mathrm{MeV}^{1/2}\mathrm{cm}^{3/2})\frac{m_a}{10^{-5}\mathrm{eV}}$, where m_a is the mass of the axion. The mass of the axion is constrained by cosmological considerations to $m_a > 10^{-5}\mathrm{eV}$ and from measurement of the cooling rates of red giants to $m_a < 10^{-2}\mathrm{eV}$. Due to this low coupling constant, axions are predicted to interact very little with ordinary matter. This low coupling constant in addition to their expected mass scale makes them prime candidates for cold dark matter.

1.2.3 MaCHOs

MaCHOs, or Massive Compact Halo Objects, are large, non-luminous celestial bodies such as brown dwarfs, black holes, and neutron stars. Since these bodies are made of entirely baryonic matter, their existence would not depend on any extension to the Standard Model, and their large masses would make them possible candidates for cold dark matter.

However, theoretical calculations of the amount of baryonic matter produced in the universe tells us that not enough baryons were produced by the Big Bang to constitute enough MaCHOs to account for the observations that motivate dark matter. While MaCHOs may constitute some amount of the measured cold dark matter in the universe, they cannot explain all of our observations, and other models are still needed to explain what we see [35].

These results were experimentally verified by the EROS collaboration, which used gravitational micro-lensing measurements to look for massive low-luminosity bodies in the galaxy. While this collaboration observed the expected number of brown dwarfs within the galactic plane, they did not find any such bodies in the Magellanic clouds, thereby ruling out the possibility of the dark matter halo being composed of MaCHOs with masses between $10^{-7}M_{\odot} < M < 5M_{\odot}$[40].

The OGLE collaboration verified these results with a similar experiment, looking for micro-lensing in the Large Magellanic Cloud. After collecting data for 10 years, OGLE only detected three candidate MaCHOs, well below the required event rate for MaCHOs to explain the dark halo and consistent with EROS. These observations place an upper limit on the contribution of MaCHOs to the total mass of the dark halo of approximately 1.7×10^{-7} [21].

1.2.4 Sterile Neutrinos

Neutrinos are leptons with very little mass that only interact via the weak nuclear force and the gravitational force. All neutrinos that are detected through nuclear reactions are observed to have left-handed chirality. Similarly, all anti-neutrinos that we observe are observed to be right-handed. The sterile neutrino is a hypothetical right-handed neutrino or left-handed anti-neutrino. Since they do not interact with the electromagnetic or strong forces but, due to their small but nonzero mass, would have a gravitational effect, sterile neutrinos are considered to be a candidate for hot dark matter.

However, since hot dark matter particles move with high velocities, they would not be able to account for the clumping in the early universe that lead to galaxy formation, and so other forms of dark matter are also needed to account for our observations.

While sterile neutrinos may exist, Abazajian et. al have shown in [34] that they cannot constitute an appreciable fraction of the total observed dark matter in the universe. By considering the production of sterile neutrinos in the early universe and their oscillation rates with other neutrino flavors, these authors found that the closure fraction of the universe for sterile neutrinos can be given by

$$\Omega_{\nu_s} h^2 \approx 0.3 \left(\frac{\sin^2 2\theta}{10^{-10}} \right) \left(\frac{m_s}{100keV} \right)^2 \tag{1.2}$$

where θ is the mixing angle for the sterile neutrino and m_s is the sterile neutrino's mass [34]. Using the recent LSND results indicating the likelihood of a sterile neutrino with mass on the order of 1 eV, the constrains placed on $\sin^2(2\theta)$ by MiniBooNE, KARMEN, and NOMAD estimating that $\sin^2(2\theta)$ be on the order of 3×10^{-3}[33], and the WMAP cold dark matter closure fraction $\Omega_c h^2 = 0.1131 \pm 0.0034$, $\Omega_{\nu_s} h^2 \approx 0.0009 << \Omega_c h^2$, showing that sterile neutrinos are account for at most .008 of the observed dark matter.

1.3 Direct Dark Matter Detection

Many detector experiments are currently running or under development in order to directly detect dark matter. Most direct searches use detectors designed to detect dark matter particles passing through them; if dark matter forms a halo around the galaxy as expected, as the earth moves through the galaxy, there should be dark matter "wind" blowing over us. When a dark matter particle passes through a detector, the particle may interact with a nucleus within the detector. After the collision, the nucleus then recoils, and the detector can detect the recoil and determine whether or not it was likely caused by a dark matter interaction.

Since dark matter is so elusive, positively identifying a signal is very hard to do. When an experiment does not manage to do this, however, it can place limits on the probability that the dark matter interacts, so that the parameter space in which these particles might exist can be narrowed down. Detectors that strive to positively identify dark matter need much higher sensitivity and lower background than those that place limits.

The standard method of placing limits on a data set is to assume that all of the measured events are background and to determine the probability that a dark matter particle with a given set of properties would not be detected within the range of values that the detector was sensitive to, given the number of background events and the model being tested. Most limit setting techniques place a limit on the interaction cross section for a given dark matter particle mass.

1.3.1 Axion Searches and ADMX

Experiments like ADMX (Axion Dark Matter eXperiment) search for axions deflecting photons in a strong magnetic field. In sufficiently strong magnetic fields, there is a nonzero probably that an axion will turn into a photon. ADMX uses an array of very high-sensitivity and low background SQUIDs (Superconducting Quantum Interference Devices) that amplify the radio-frequency power associated with this photon in order to detect axions.

The kinetic behavior of axions is described by the Standard Model Lagrangian modified to account for interactions with the "hidden sector" of particles that are not easily detectable:

$$\mathcal{L} = -\frac{1}{4}F^{\mu\nu}F_{\mu\nu} - \frac{1}{4}B^{\mu\nu}B_{\mu\nu} - \frac{1}{2}\chi F^{\mu\nu}B_{\mu\nu} + \frac{1}{2}m^2 B^{\mu}B_{\mu} \tag{1.3}$$

Here, $F^{\mu\nu}$ is the electromagnetic field strength tensor, $B^{\mu\nu}$ is the hidden sector field strength tensor, χ is the kinetic coupling—a parameter that controls the probability of an axion turning into a photon—m is the mass of the axion, and B^{μ} is the hidden sector vector potential of the axion.

In November 2010, ADMX published a limit on axions excluding vector bosons with kinetic couplings $\chi > 3.48 \times 10^{-8}$ for masses less than $3\mu\text{eV/c}^2$[13]. Figure 1-5 shows experimental limits on these parameters.

1.3.2 WIMP Searches

Since WIMPs are predicted to interact via the weak force, they can be detected through low-probability collisions with target nuclei. Using noble liquids as a detection medium has become a popular paradigm among many current detectors, such as LUX, XENON100, and MiniCLEAN. However, other methods of detection are also explored by groups such as CDMS and DM-TPC.

Figure 1-10 summarizes results from several experiments that have placed limits on the WIMP cross section versus mass distribution, as well as limits that are projected to be set by several future experiments.

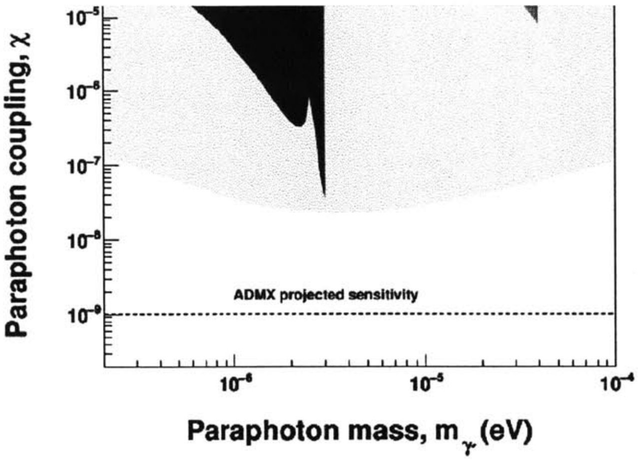

Figure 1-5: Paraphton coupling constant versus mas (in eV). Excluded regions of paraphoton (e.g. axion) kinetic coupling and mass parameter space. The dark region is the most recent limits placed by ADMX. The light gray shading is the limits placed by an earlier microwave cavity experiment, and the light shading comes from deviations from Coulomb's law [13].

1.3.3 Event Rates

The rate at which the detector should measure WIMP scattering events depends on the flux of the dark matter passing through the detector, the probability of a given WIMP interacting with a target nucleus in the detector as it passes through, and the efficiency of the equipment for actually measuring an interaction when it occurs. Assuming 100% equipment efficiency, the differential rate per unit mass of WIMPs interacting is given by

$$\frac{dR(v_E, v_{esc})}{dE_r} = k\frac{R_0}{E_0 r}\left(\frac{\pi^{1/2}}{4}\frac{v_0}{v_E}\left[\mathrm{erf}\left(\frac{v_{min}+v_E}{v_0}\right) - \mathrm{erf}\left(\frac{v_{min}-v_E}{v_0}\right)\right] - \frac{R_0}{E_0 r}e^{-v_{esc}^2/v_0^2}\right) \tag{1.4}$$

k is a normalization constant, normalizing the number of WIMPs for their velocity, given by

$$k = \left[\mathrm{erf}\left(\frac{v_{esc}}{v_0}\right) - \frac{2}{\pi^{1/2}}\frac{v_{esc}}{v_0}e^{-v_{esc}^2/v_0^2}\right]^{-1} \tag{1.5}$$

v_{esc} is the escape velocity for the galaxy (i.e. the highest velocity a galactic WIMP would have, generally around 600 km/s), v_E is the velocity of the Earth, given by

$v_E \approx 244 \pm 15$ km/s, depending on the time of the year, v_{min} is the velocity of the dark matter particle with the minimum energy to produce a recoil with energy E_r. v_{min} is given by

$$v_{min} = \left(\frac{E_r}{E_0 r}\right)^{1/2} v_0 \tag{1.6}$$

v_0 is the average dark matter velocity corresponding to average dark matter energy E_0, r is a kinematic factor and is given by

$$r = \frac{4M_D M_T}{(M_D + M_T)^2} \tag{1.7}$$

where M_D is the WIMP mass and M_T is the target nucleus mass. R_0 is interaction rate at zero momentum transfer, given by

$$\frac{R_0}{r} = 126\left(\frac{\sigma_0}{1\mathrm{pb}}\right)\left(\frac{1\mathrm{GeV/c^2}}{\mu}\right)\left(\frac{\rho_D}{0.4\mathrm{GeVc^{-2}cm^{-3}}}\right)\left(\frac{v_0}{230\mathrm{km/s}}\right) \tag{1.8}$$

where μ is the reduced mass of the WIMP and the target nucleus, ρ_D is the density of the dark matter, between 0.3 $\mathrm{GeVc^{-2}cm^{-3}}$ and 0.7 $\mathrm{GeVc^{-2}cm^{-3}}$, with a generally accepted value of 0.4 $\mathrm{GeVc^{-2}cm^{-3}}$, and σ_0 is the zero momentum transfer cross section. This is related to the energy dependent cross section σ by

$$\sigma = F(q)^2 \sigma_0 \tag{1.9}$$

where $F(q)$ is the nuclear form factor for a recoil momentum q. The form factor describes the nuclear physics associated with how the dark matter particle will scatter off of a nucleus rather than just one nucleon. For spin-independent interactions, the form factor is given by,

$$F(q) = 3\frac{j_1(qr_n)}{qr_n} e^{-(qs)^2/2} \tag{1.10}$$

where r_n is the radius of the target nucleus ($r_n \approx 1.14A^{1/3}$ fm), $j_1(x)$ is the first order Bessel function, and s is the nuclear skin thickness ($s \approx 0.9$).

The WIMP-nucleon cross section is determined by the particle physics of the

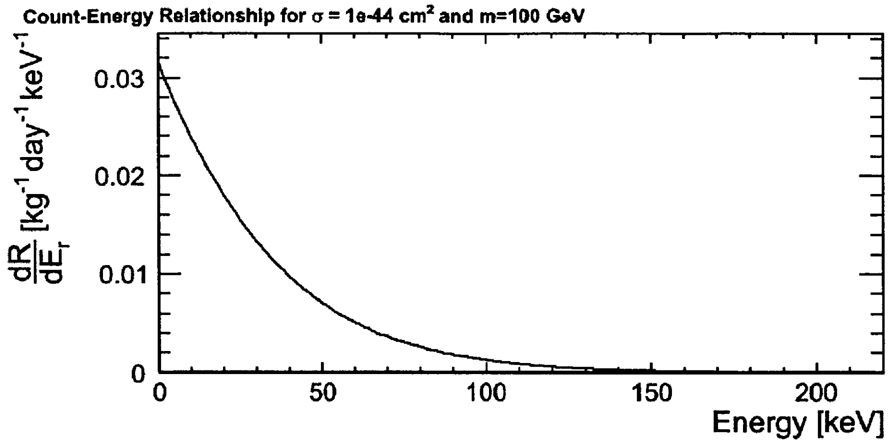

Figure 1-6: Differential rate of WIMP interactions per recoil energy (in kg^{-1}days^{-1}keV^{-1}) versus recoil energy (in keV) for 100 GeV WIMPs scattering in a liquid argon detector with a cross section of 1×10^{-44} cm^2. Scaling the y-axis by the total exposure during an experiment (in kilogram-days) and integrating over the recoil energy region of interest gives the total number of recoil events that the experiment is expected to detect.

interaction and obeys

$$\sigma \propto \left(\frac{g_D^2 g_N^2}{M_E^4}\right) \mu^2 \tag{1.11}$$

where g_D and g_N are the coupling strengths of the WIMPs and the target nuclei, respectively, and M_E is the mass of exchange particle moderating the interaction. Since g_N is proportional to A, the mass number of the target nucleus, we find that $\sigma \propto A^2$, and therefore that the zero momentum transfer cross section per unit mass and rate per unit mass are both proportional to A^2. Since A is a property of the target nucleus and is not an interesting part of the dark matter physics, we normalize the results of our experiment by giving the per nucleon rates and cross sections by dividing the measured quantities by A^2 so that they can be compared to other experiments [37].

The differential interaction rate as described in [37] for a 100 GeV WIMP interacting in a liquid argon detector with cross section 1×10^{-44} cm^2 is shown in figure 1-6. This graph shows the shape of the recoil energy deposition distribution that WIMP detectors will be measuring data from.

Germanium Bolometer Detectors

Experiments such as CDMS, CRESST, Edelweiss, and CoGeNT use germanium bolometer detectors to detect WIMP interactions. These detectors measure ionization caused by the WIMP-nucleon interactions and compare the amount of ionization to the amount of vibrations produced by the interaction in order to distinguish nuclear recoil signals from background..

Figure 1-7 shows the limits published by CDMS II for the WIMP mass versus WIMP-nucleon cross section [26]. CDMS is currently the leading germanium bolometer experiment in terms of dark matter sensitivity.

Other Detection Methods

The DAMA/LIBRA (Large sodium Iodide Bulk for RAre processes) experiment uses 250 kg of NaI crystals surrounded by photomultiplier tubes to detect WIMP interactions. When a nuclear recoil occurs within the detector, a burst of photons is produced that is detected by the photomultiplier tubes. While these signals can come from WIMPs or from background sources, DAMA/LIBRA looks for long term signal modulation to differentiate between these two types of signals [23]. Since the Earth is moving around the sun, the velocity of the Earth with respect to the dark halo changes over the course of a year. This means that the dark wind (and therefore the incident WIMP flux) changes periodically as well. By collecting data for several years and recording the signal strength over time, they were able to detect an annual modulations with recoil energies from 2–6 keV with modulation depth of 2%, differing from the null hypothesis of no modulation by 8.2σ [22]. The possible allowed regions of dark matter parameter space from this experiment are shown in figure 1-7.

DM-TPC, the Dark Matter Time Projection Chamber is a direction-sensitive detector being developed that uses gaseous CF_4 as a detection medium. Although using gas decreases the total target mass, DM-TPC's ability to measure the tracks of incident WIMPs makes it able to substantially reduce the number of background events by only considering tracks that appear to come from the Cygnus constellation, the direction in which we expect the dark matter wind to be flowing over the earth [20].

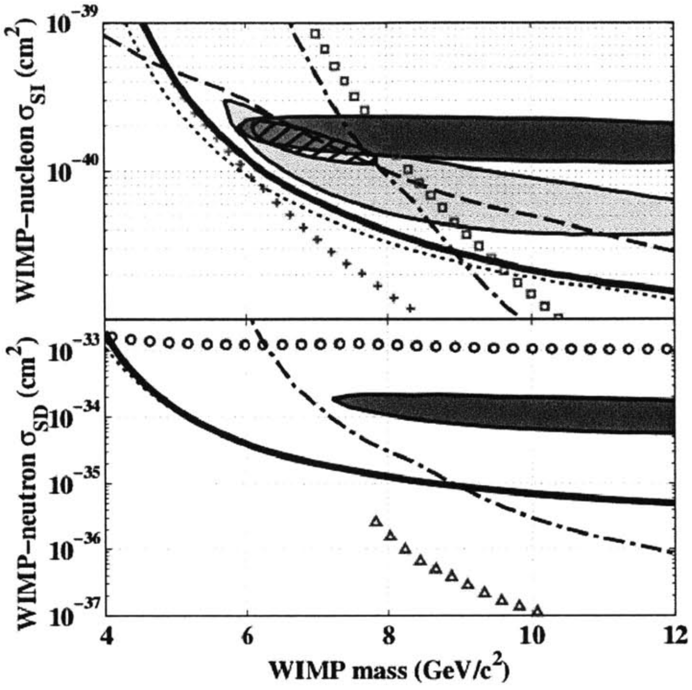

Figure 1-7: The current WIMP-nucleon cross section versus WIMP mass as placed by CDMS in [26]. TOP: These curves all demarcate the minimum spin-independent cross sections that WIMPs can have at each given mass. The dark solid line shows the results found from CDMS II, the dashed line shows the results from a low-threshold analysis of CDMS II shallow-site data, the dash-dotted curve shows the CDMS II results with a 10 keV threshold, the + and □ denote the results published by XENON100 with, respectively, constant and decreasing scintillation efficiencies at low energies, the light shaded region is a region of possible signal found by CoGeNT, and the dark shaded region is a similar region found by DAMA/LIBRA; the hashed region is a combined fit to the results of CoGeNT and DAMA/LIBRA. BOTTOM: These curves show the spin dependent limits from the same data, with the solid line showing the results of the data from CDMS II, the dash-dotted line shows the CDMS II results with a 10 keV threshold, the △ are the results from XENON10, the ○ are the results from CRESST, and the shaded region is the 99.7% confidence level region of neutron-only scattering found by DAMA/LIBRA. [26]

Liquid Noble Gas Detectors

Liquid noble gas detectors currently have the leading dark matter sensitivity, as shown by the XENON100 results in figure 1-7. Because noble gases have very few chemical self-interactions, they have less intrinsic background than many other liquid or gaseous media. Additionally, separation processes can be used to clean noble gases down to very low radioactivities, lowering the detectors' background rates and improving their sensitivities [4].

One of the biggest advantages of noble liquid detectors, is their ability to distinguish between background electronic recoils and nuclear recoils, the type of recoil we expect to see from signal WIMP interactions. When a particle collides with a noble liquid atom, the atom recoils and is ionized if the projectile energy is above the ionization energy of the atom. This initial ionization releases light that can be detected by photomultiplier tubes. When the ion collides with another atom, they briefly bond together, forming a dimer. However, since noble gases are most stable when not chemically bound to any other atoms, the dimer will eventually split apart, releasing light that can be also be detected.

When the dimer forms, the two atoms may bind together to form either a triplet or singlet state. The triplet has a significantly longer lifetime than the singlet state (lifetimes for both states for a few liquid noble gases are listed in table 1.1), so the decay of the triplet states can be easily differentiated from the decay of the singlet states by the time distribution of the detected scintillation light. Nuclear recoils have higher energy densities and produce more interactions that destroy the triplet state, and so nuclear recoils will be distinguished by a higher prompt light fraction [45]. This way of differentiating between nuclear and electronic recoils is called pulse shape discrimination.

Target Nucleus	Singlet Lifetime (ns)	Triplet Lifetime (ns)
Ne	$< 18.2 \pm 0.2$	14900±300
Ar	7.0±1.0	1600±100
Xe	4.3±0.6	22.0±2.0

Table 1.1: Liquid noble gas dimer lifetimes, from [45]

It has been experimentally shown in [4] that this pulse shape discrimination has a background rejection power of 10^8, and can be used for liquid argon detectors to achieve a minimum WIMP-nucleon cross section of 10^{-43} cm^2 for 100 GeV/c^2 WIMPs incident on a 2 kg liquid argon target for a year. If the volume of the liquid argon is scaled up to the tonne scale, then a sensitivity of 10^{-46}cm^2 can be achieved.

Different liquid noble gas detectors under development use different elements primarily because of their nuclear properties. The interaction cross section for a given nucleus is proportional to the nuclear mass squared, meaning that heavier nuclei are expected to have significantly higher event rates than lower nuclei. However, lighter nuclei pick up more momentum in a collision, resulting in higher energy nuclear recoils which can be easier to detect, and so produce more light in an interaction. Other factors that go into choosing a detector medium include the price of the medium, as it may be more feasible to scale a detector with a cheaper medium up to the tonne scale than with a more expensive medium, and the intrinsic radioactivity of the medium.

LUX (Large Underground Xenon detector) and XENON100 are both liquid xenon detectors that will use this pulse shape discrimination to eliminate noise from electronic recoils. In 2007, XENON10, the predecessor to XENON100 placed a 90% confidence level upper bound on the WIMP-nucleon cross section at 8.8×10^{-44}cm^2 for a WIMP of mass 100 GeV/c^2 and 4.5×10^{-44}cm^2 for a WIMP of mass 30 GeV/c^2 [19]. XENON100 has recently published an even stronger limit, excluding WIMPs with cross sections above 7×10^{-45}cm^2 for WIMPs with mass 50 GeV/c^2 [16].

The DEAP/CLEAN Collaboration is currently working on two lines of liquid argon detectors: the DEAP (Dark matter Experiment using Argon Pulse-shape discrimination) series and the CLEAN (Cryogenic Low-Energy Astrophysics with Noble gases) series. The DEAP detectors all use liquid argon as a detection medium, while the CLEAN detectors can use liquid argon or liquid neon. Both detectors are currently on their second generations: DEAP-3600 and MiniCLEAN, the latter of which will be the focus of this thesis. Further details of the MiniCLEAN detector will be discussed later in Section 1.4.

MicroCLEAN, the prototype to MiniCLEAN, was a 3.14 kg detector that used liquid argon and liquid neon. It measured the effectiveness of pulse shape discrimination for differentiating between nuclear and electronic recoils in these media, and measured the nuclear recoil scintillation efficiencies within these materials. MicroCLEAN used two photomultiplier tubes to measure an energy resolution in liquid argon at 41.5 keV of 8.2%[25]. After confirming that the design had adequate energy resolution, the collaboration began designing MiniCLEAN, the following generation, 150 kg fiducial volume, detector.

1.4 MiniCLEAN

MiniCLEAN is a WIMP detector being developed by the DEAP/CLEAN collaboration. MiniCLEAN is now under constructoin at SNOLAB (Sudbury Neutrino Observatory Laboratory) and will be completed by early 2012. A drawing of MiniCLEAN is shown in figure 1-9. MiniCLEAN consists of an inner vessel containing either liquid argon or liquid neon surrounded by 92 photomultiplier tubes. The inner vessel rests inside of an outer vessel which rests in the center of a water tank.

The purpose of the outermost water tank is to block incoming radiation from external sources. The inner vessel of MiniCLEAN contains 500 kg of liquid argon or 430 kg of liquid neon, while the fiducial volume is restricted to 150 kg. The fiducial volume radius is 29.5 cm, outside is a neutron-absorbing region that extends to a radius of 44 cm. A 10 cm layer acrylic surrounds this volume to increase the neutron absorption, and the photomultiplier tubes are at a radius of 73.5 cm. Only events that occur within the fiducial volume will be considered candidates for WIMP interactions. The much greater volume of argon or neon and acrylic that surrounds this volume will shield the fiducial volume from most of the incident background neutrons and α particles. Simulations, as will be discussed in Chapter 4, show that this blocking method, not including the water tank, only allows 0.5% of the total incident neutrons to interact in the fiducial volume.

When a WIMP interacts with a nucleus inside the detection medium, ultraviolet light with wavelength between 60 and 200 nm is released. This light passes through a sphere coated in tetraphenyl butadiene (TPB), a wavelength shifter that brings the ultraviolet light into the visible spectrum. The shifted light is detected by the photomultiplier tubes that surround the medium. The TPB produces 882±210 photons per MeV under alpha particle excitation with a double exponential decay with lifetimes 11±5 ns and 275±10 ns [44]. Figure 1-8 shows the emission spectra of TPB, measured for several incident wavelengths.

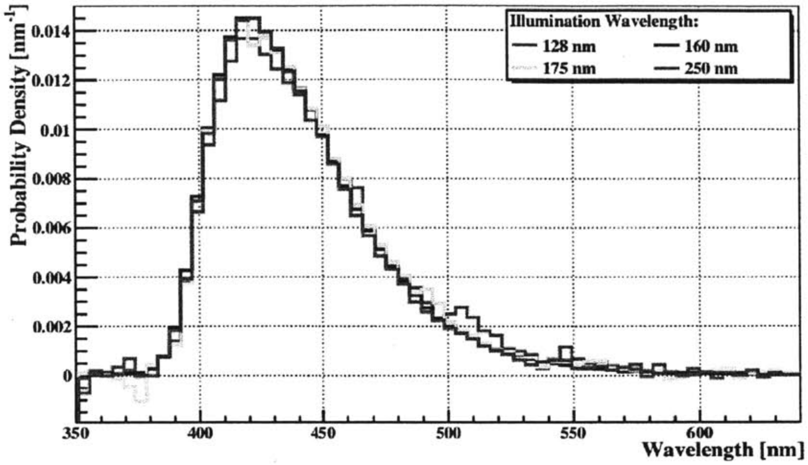

Figure 1-8: Probability density (in nm^{-1}) versus wavelength (in nm). This graph shows the visible re-emission spectra for extreme ultraviolet photons of four different frequencies incident on TPB, normalized to unit area. [24]

Additionally, MiniCLEAN reduces its internal background by its choice of materials. Some internal background comes from the decay of radioisotopes in the detector materials. Since neon does not have any radioisotopes and argon can be purified to very low radioactivities [15], both media have very low internal background—especially if depleted argon is used for argon experiments—increasing the confidence with which they can detect WIMP interactions. However, when depleted argon is not used, whatever ^{39}Ar is not purified from the medium will still provide a background of 1 Bq per kg of natural argon [42]. The other major source of background comes from external neutrons and is discussed in Chapter 4.1.1. Since MiniCLEAN can use argon or neon, it can look for WIMPs with both media in order to help verify its own results.

The tube down which the calibration neutron source will be deployed extends down the port in the outer vessel labeled A in figure 1-9. In order to maximize the number of neutron interactions detected, the neutron source will be deployed as close as possible to the inner vessel, which is tangent to the outer edges of the

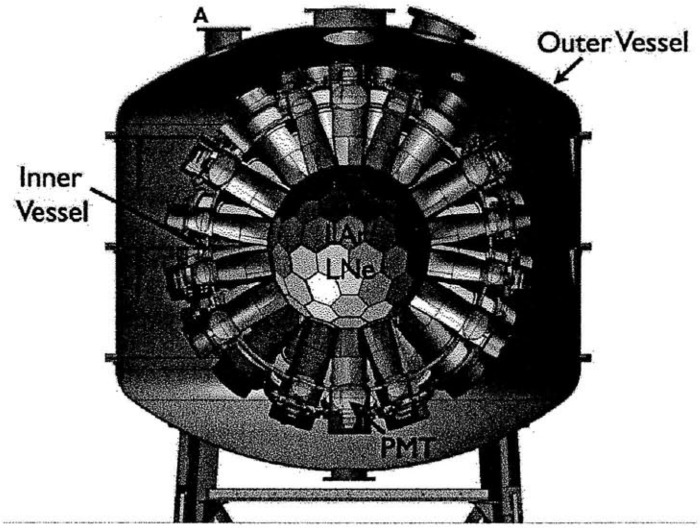

Figure 1-9: A drawing of MiniCLEAN, generated by James Nikkel for the August 2009 SNOLAB workshop. The calibration tube (not shown) enters the outer vessel at the port labeled A.

photomultiplier tubes. The tube runs outside of the inner vessel rather than through the argon or neon so that the volume of the calibration tube does not detract from the background-shielding liquid that would be in its place; instead, when the tube is external to the medium, the calibration process can also measure the effectiveness of the medium's self shielding. Placing the neutron source outside of the inner vessel also ensures that the tube will remain tangent to the photomultiplier tubes, so that the spatial distribution of calibration neutrons incident on the detector will be more predictable.

Since MiniCLEAN's operative components are a large sphere of low-radioactivity material surrounded by photomultiplier tubes, it scalable to larger volumes, with few major design changes needed. After MiniCLEAN runs and has results, it will ether detect WIMPs, in which case a bigger detector will be needed to further investigate their nature, or it will not detect WIMPs, in which case a bigger detector will be needed to reacher greater sensitivities. For this reason, the DEAP/CLEAN collaboration plans on developing CLEAN, the next generation of the CLEAN series, to detect WIMPs at an even greater sensitivity. Figure 1-10 shows the expected sensitivity of MiniCLEAN plotted alongside the projected sensitivity for CLEAN with neon, argon, and depleted argon media. The sensitivity curves for a few other experiments are also plotted alongside these curves for comparison.

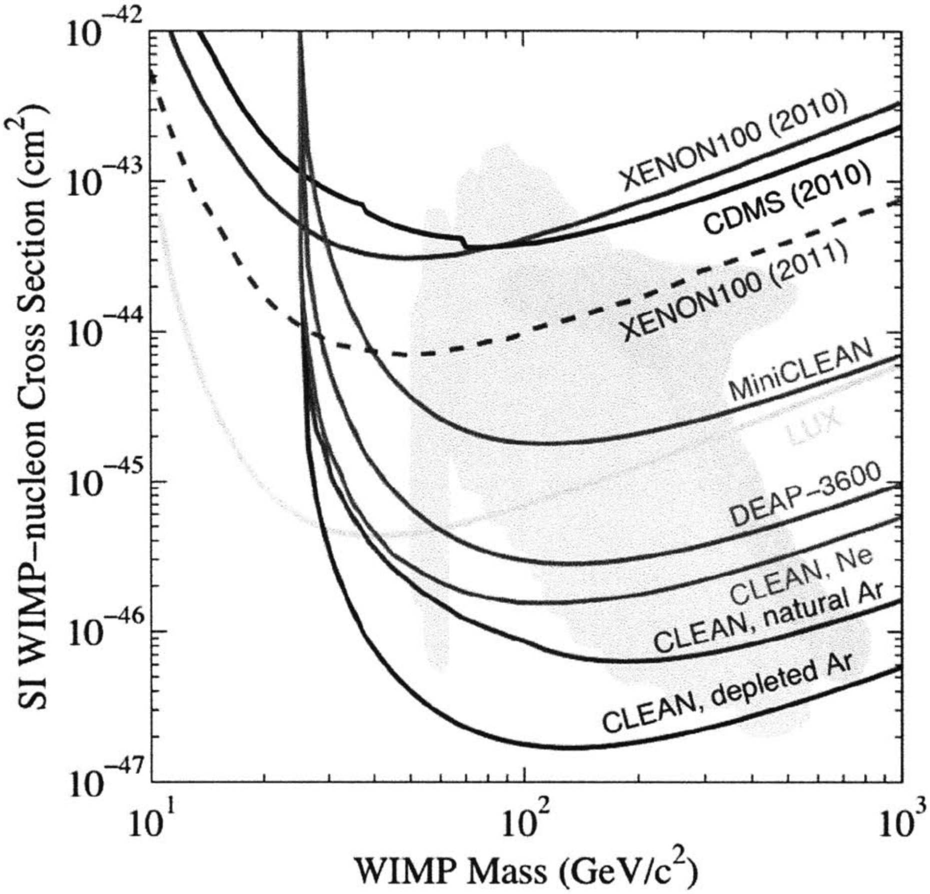

Figure 1-10: Measured and projected sensitivity curves for several different dark matter experiments.

Chapter 2

Calibration Deployment System

The MiniCLEAN neutron source calibration process will consist of lowering the neutron source through the water tank into the ouer vessel, pulsing the neutron source for a specified amount of time, recording the neutron induced nuclear recoil spectrum as measured by the photomultiplier tubes, and removing the neutron source from the tank. The neutron source is deployed through a continuous tube, as shown in figure 2-1, leading through the water tank and into the outer vessel, adjacent to the photomultiplier tubes, so that the neutron source may be lowered right next to the inner vessel. The neutron source will be contained in a canister (described in Chapter 3.2) that will be lowered by a winch. In order to precisely control the deployment, the process is fully automated, and a controller was designed to control the winch from a computer. The details of each part of the deployment system are discussed in this chapter. Figure 2-2 shows a design drawing of the winch mounted on the deployment test stand. The motor is shown in yellow in this image. The HV supply goes in the rectangle attached to the winch. The HV supply is mounted on the rotating part of the stand so that the umbilical cable coming out of the HV supply will not twist and tangle. The red object is a liquid joint that allows the HV supply to spin while its power source is plugged into the back end.

Figure 2-3 shows a picture of the completed winch and deployment system setup.

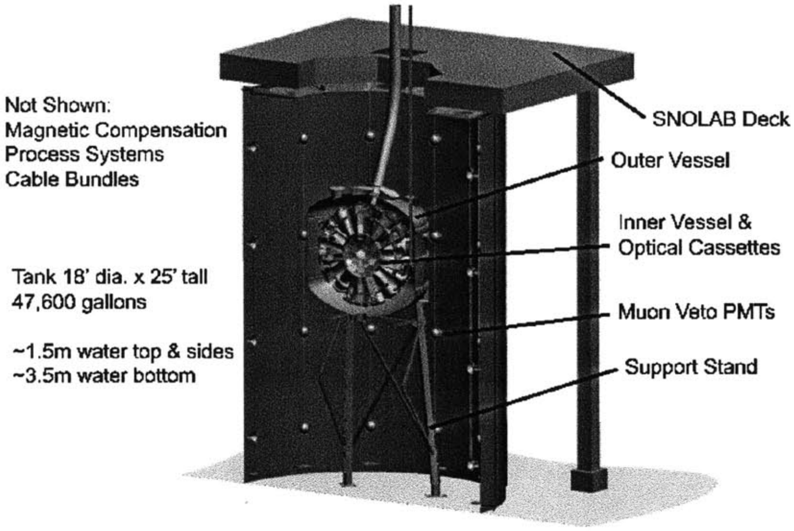

Figure 2-1: A cross section picture of MiniCLEAN. The water tank, muon veto photomultiplier tubes, inner and outer vessels, photomultiplier tubes, calibration tube, and stands are shown. The long (3.54 m) cylinder (in red) that enters the outer vessel on the top right is the calibration tube that the neutron source will be deployed down.

2.1 Cables

The winch holds the canister by a thin, load-bearing steel cable. Another thicker but not load-bearing umbilical cable attaches to the canister to supply power to the neutron source inside. Both cables are wound around the drum of the winch and remain attached to the canister as it is lowered. Since the steel cable is thinner than the umbilical cable, it will unwind more slowly. This has the effect that after lowering several feet, the umbilical cable will begin to build up excessive amounts of slack that will prevent the canister from moving down the narrow deployment tube smoothly. Figure 2-4 shows the calculated slack build up between the umbilical wires and the steel cable as the winch spins, showing that by the time the winch has lowered the canister 15 feet, several feet of slack have already built up. To avoid this problem, the steel cable and the umbilical are attached to each other with cable sleeving so that they will be forced to deploy at the same rate.

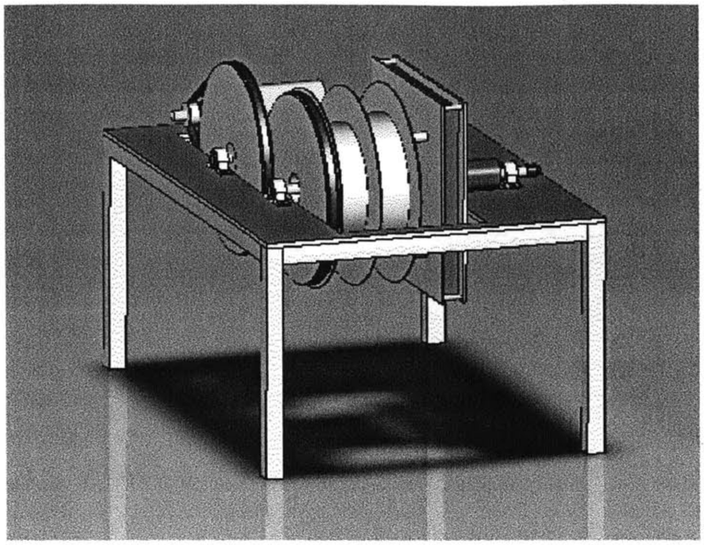

Figure 2-2: A CAD drawing of the winch on its stand.

2.2 Motor

The winch is controlled by a three phase reversible motor, a diagram of how this works is shown in figure 2-5. The motor takes as input three AC signals of equal amplitude but different phases. The current from each input runs through a coil around a ferromagnetic core. This current causes the core to become magnetized in proportion to the amplitude of the AC current at any point in time. Since the three inputs are at different phases, the magnetic fields produced at each coil peak and reverse polarity at different times. That means that with the three coils places around a circle, a magnet in the center will continue to spin in circles as the polarities of the coils change, thus spinning the motor.

A 2 inch diameter gear connecting to the motor spins a belt drive to turn a 20 inch diameter gear. This 20 inch diameter gear is directly connected to a 2 inch diameter gear, which spins another belt to turn another 20 inch diameter gear, making the final gear spin at $\frac{1}{100}$ the speed of the motor. This last gear spins the drum of the winch. The speed of the winch can be controlled by changing the sizes of these gears. The current gear ratios were chosen in order to lower the canister at a rate of approximately one inch per second.

The motor is controlled by the controller, which accepts the positive and nega-

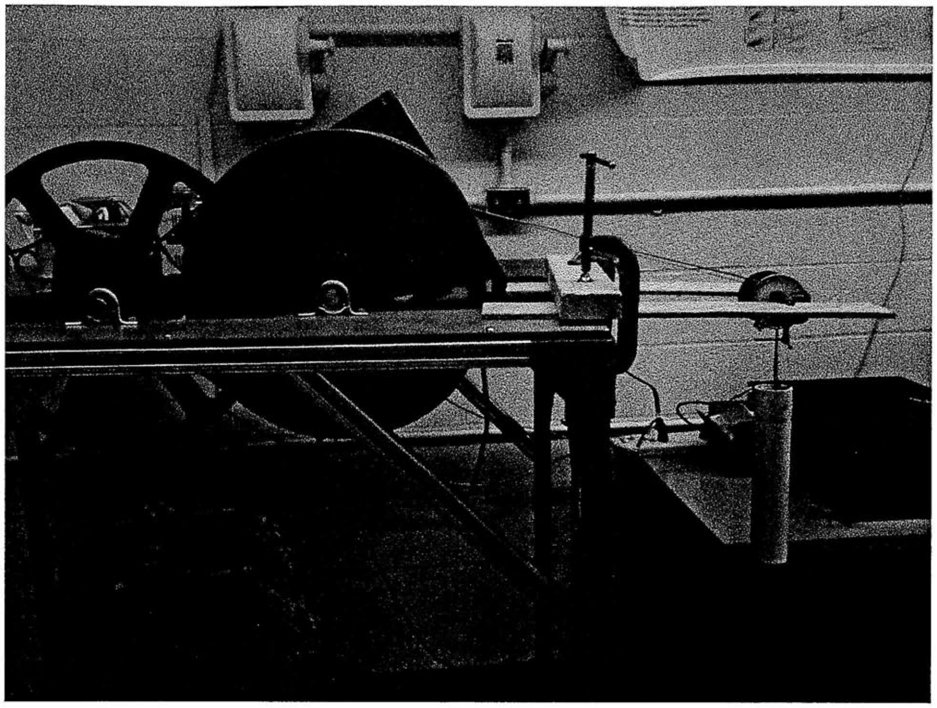

Figure 2-3: A photograph of the winch in its stand, connected to the computer and ready for operation. Wooden panels were added to lower the canister from an arm rather than its usual position directly below the front of the winch. These panels were added to facilitate indoor testing over short distances.

tive leads of wall power and runs one lead through a high voltage 60μF capacitor, introducing a phase shift. This is used to control the motor direction, and thereofre whether the canister is being raised or lowered. For example, if we say that the positive lead of the wall power is at a 0° phase shift, the negative lead is at a 180° phase shift and the end running through the capacitor is shifted by approximately 60°. By interchanging the 0° and 60° wires, we can reverse the direction that the motor spins. A drawing of the overall control structure is shown in figures 2-8 and 2-9, where the circuits that raise and lower the canister are shown separately, controlled by the relays.

2.3 Controller

A LabJack USB DAQ (the high voltage-rated U3 model with 16 flexible — digital input or output — ports and 2 analog outputs) connects the controller to the com-

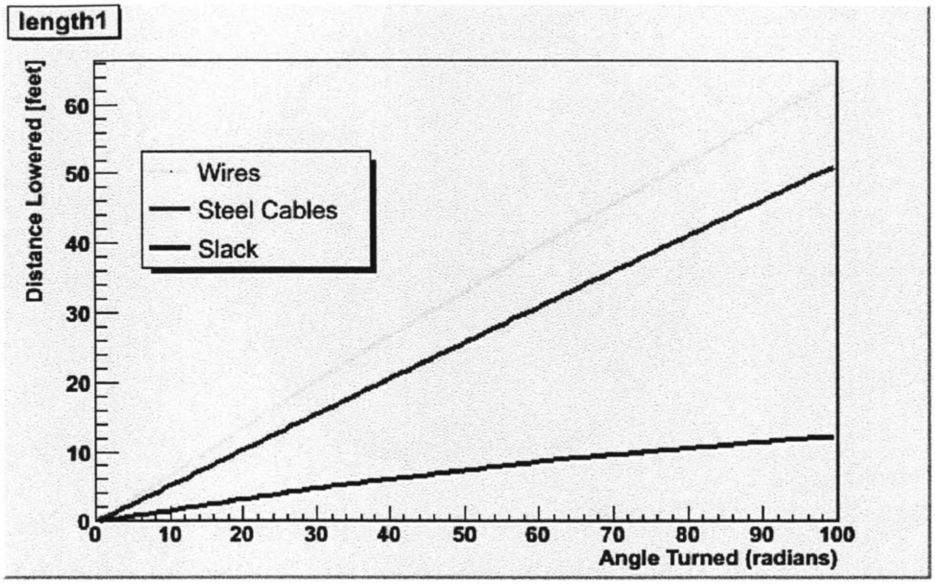

Figure 2-4: The buildup of slack between the umbilical cables (labeled wires) and load-bearing steel cable as the winch spins. The distances shown on this graph go far beyond the expected deployment distances so that the overall effects can be seen more clearly; however, signficant slack builds up by the time the canister has been deployed the 15 feet that we expect to deploy it. This buildup was made assuming the idealized conditions of a perfectly clean wrapping of the cables, where none of the cables wrap on top of each other and they unwind smoothly as the canister is lowered.

puter, so logic signals from the computer can be sent to the controller. See Appendix E for the specifications of the LabJack. The first part of the circuit controls power to the winch. The default is for the motor to be turned off. When the computer signals for the motor to turn on, the LabJack sends 1V to a transistor, which opens up and allows a 24VDC source to power a relay, which then completes the circuit and allows power to reach the motor. When the motor is turned off in software, the computer ceases the 1V signal, the transistor closes, and the relay is turned off, no longer powering the motor.

After passing the on/off section of the circuit, the positive end of the wall power splits, sending half through a large 60 μF capacitor and introducing the phase shift needed to drive the motor. When power is supplied to the motor, the default is for it to lower the canister. Hence, the default configuration for the wires passing through the relays has the 0° and 60° wires ordered to spin the winch to lower the canister.

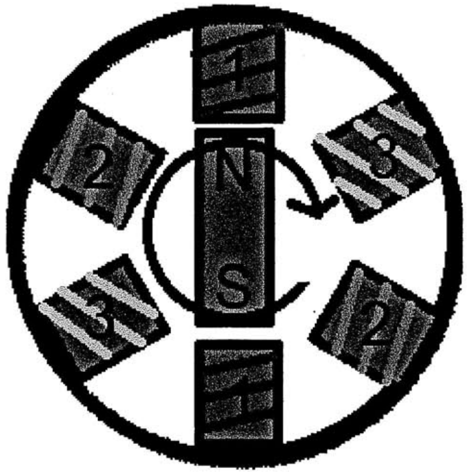

Figure 2-5: A diagram depicting a three phase motor. In the center of the motor is a magnet surrounded by three pairs of coils. Each pair of coils has a current running through it at a different phase, such that each pair creates a magnetic field that rotates the central magnet towards those coils at different times. The net effect of all three pairs of coils magnetizing out of phase is that the central magnetic is constantly being rotated between the pairs of coils, causing the motor to spin quickly and reliably.

To raise the canister, the computer sends a 1V signal through the LabJack to a transistor, which then opens allowing the 24VDC power supply to switch another relay that reorders the 0° and 60° wires, so that the winch spins in the opposite direction. 2-8 and 2-9 depict the change in controls when the relays are turned on and off to raise and lower the canister. Figure 2-7 is a photograph of the control circuit with the capacitor and relays highlighted.

2.4 Yo-Yo Potentiometer

In order to control the depth that we lower the canister to, we use a yo-yo potentiometer to measure the canister's displacement. We used the Celesco P9101 Cable-Extension Position Transducer yo-yo potentiometer, the technical specifications for which are given in Appendix F. The yo-yo potentiometer consists of a path of a material with constant resistivity. One end of a circuit is fixed to the base of the path, and the other is spring-loaded and connected to a wheel around which a long cable is wound. As the cable is extended, the wheel spins and the mobile end of the circuit moves along the path, causing the total resistance between the two ends to linearly

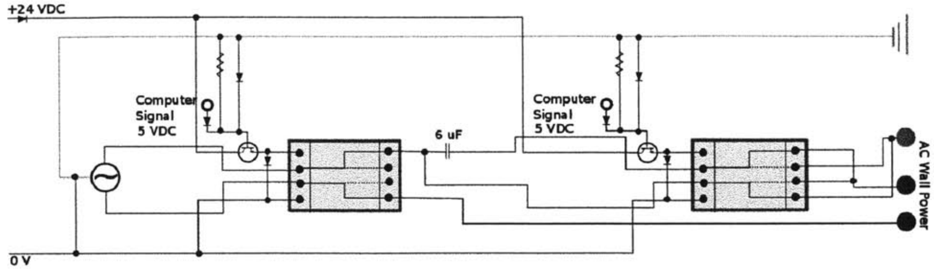

Figure 2-6: Diagram depicting the circuitry of the winch motor control system. The cyan boxes are 24V relays.

increase as the cable is unwound. The yo-yo potentiometer then outputs the difference between the voltages of the two leads. By calibrating the yo-yo potentiometer against known displacements, we can map voltage readings from the yo-yo potentiometer to extended cable lengths by considering the increasing voltage difference. The results of this calibration are shown in figure 2-10, where we can see that two different calibrations done over a long distance several months apart lead to nearly identical calibration curves. The fit parameters for both calibration runs are shown in table 2.1. The offset parameter, representing the y-intercept of the fit, differs by 0.014σ between both runs, and the slopes of each line differ by 0.013σ, showing that the results from both calibration runs are within error of each other.

Calibration Run	Slope (V/m)	Offset (V)
August 2010	0.5698±0.0007	0.0807±0.0061
November 2010	0.5568±0.0008	0.0942±0.0053

Table 2.1: Fit parameters for the yo-yo potentiometer calibration data taken in August 2010 and November 2010, shown in figure 2-10. The data for each set was fit with a line of the form $Offset + Slope \times Distance$, where $Offset$ and $Slope$ are the fit parameters.

The yo-yo potentiometer rests next to the winch on the stand and connects to the canister so that the position of the canister can be measured by measuring the change in displacement of the yo-yo potentiometer from its initial fully-wound position.

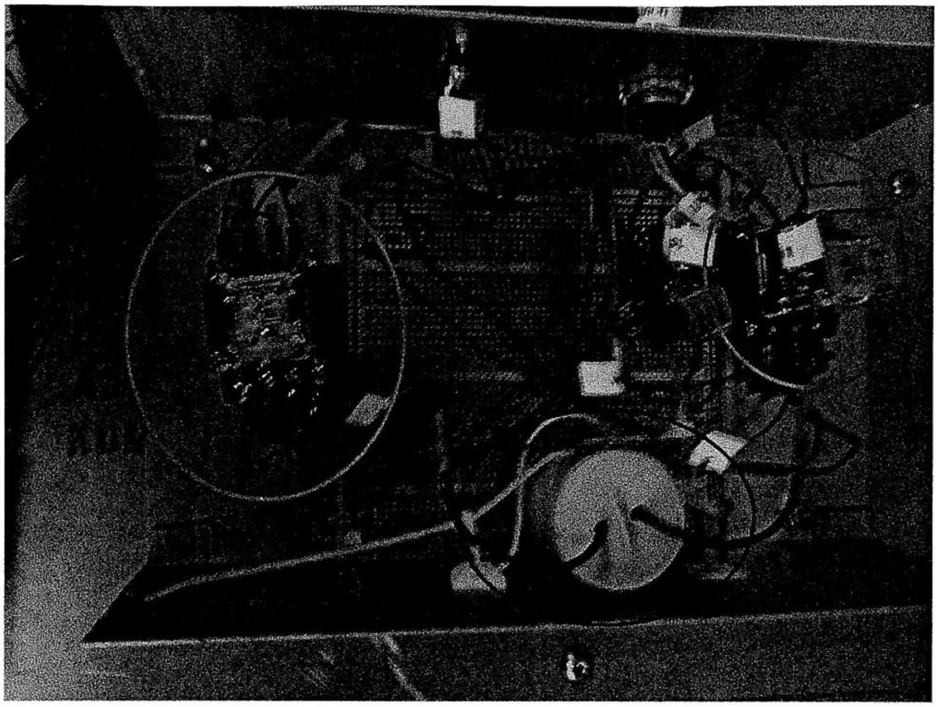

Figure 2-7: A photograph of the control circuit. Circled in red are the relays. Circled in blue is the 60μF capacitor.

2.4.1 Repeatability

The repeatability of the yo-yo potentiometer measurements was tested by lowering the canister for a minute and a half, recording the distance measured by the yo-yo potentiometer 40 times every second as the canister lowers, and repeating this process three times. The results can be seen in figure 2-11 where the measurements from all three runs are superimposed on each other. As this figure makes clear, the three sets of measurements were all so close that they cover each other on the graph. To better understand how the three runs varied, they were averaged together and their residuals from the average were plotted in figure 2-12. As this figure shows, the residuals were almost entirely within less than 0.01 inches, leaving us safely within the error margin of 0.5 cm for the deployment system.

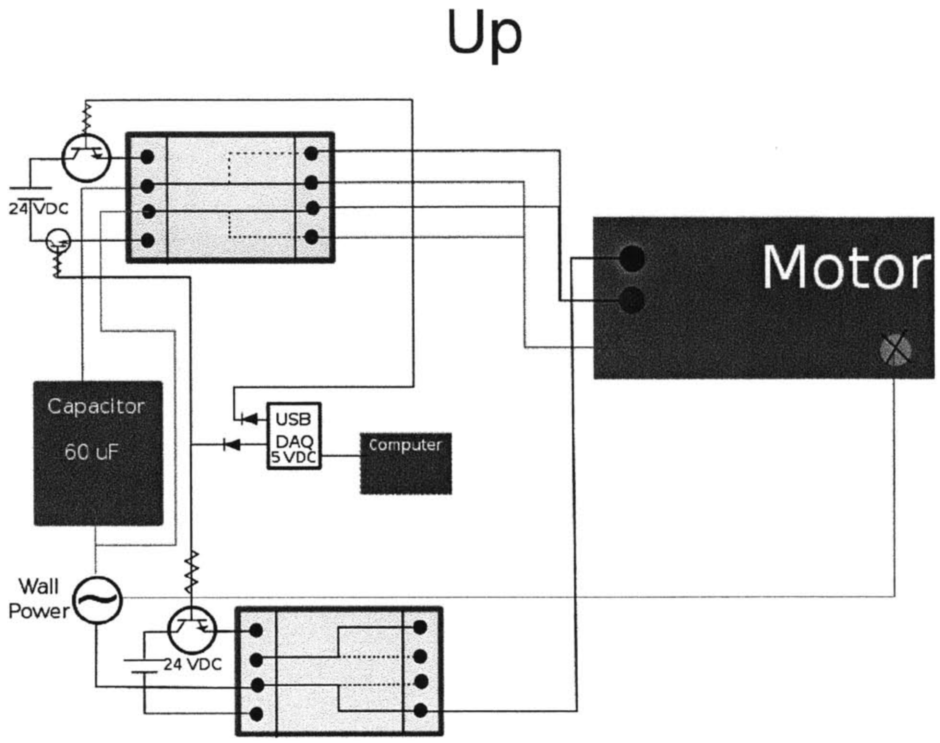

Figure 2-8: Circuit and relay configuration to raise the canister

2.5 Software

The calibration will be controlled by a program that will automate the entire process. Separate pieces of code were originally written to control the movement of canister and to turn the neutron source on and off and to collect data. A master program will make use of these three pieces to tell the canister to move to a specific set of locations, will turn the neutron source on for the desired amount of time so that the detector can collect the appropriate calibration data, then turn the source off and raise the canister. Functions that interface with the LabJack to control the canister position are found in Appendix G.

2.6 Deployment Test

In order to test the winch deployment system under more realistic conditions, we brought the winch to a high bay where were able to practice deploying the cannister

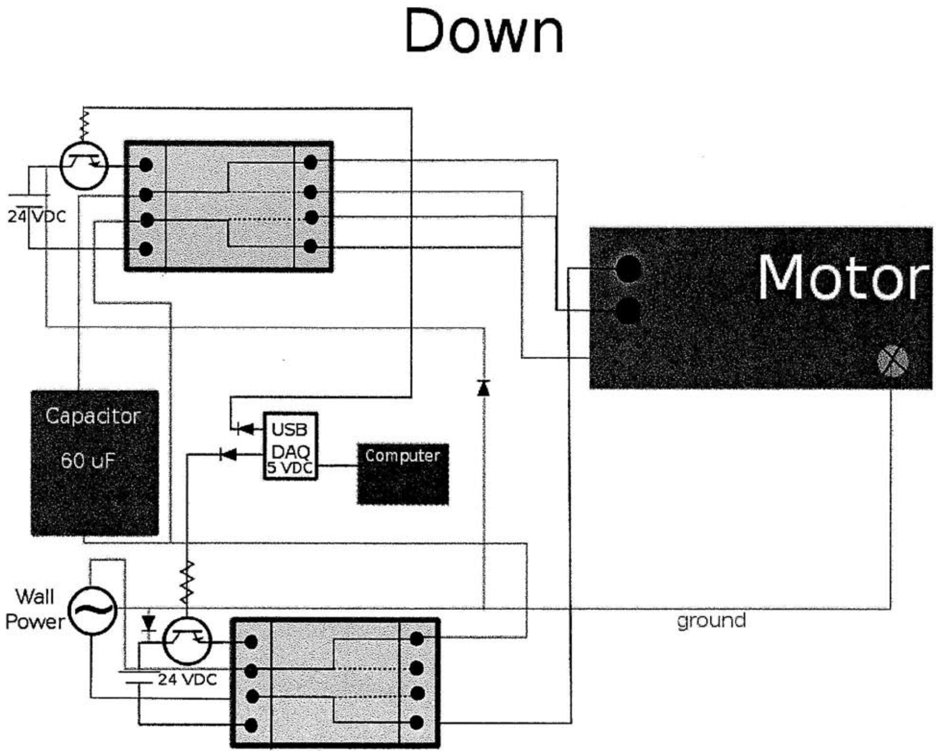

Figure 2-9: Circuit and relay configuration to lower the canister

over an eight foot descent. In order to reach the desired height, we lifted the deployment stand several feet into the air using a fork lift, as shown in figure 2-13. We tested the deployment several times, lowering the canister freely, and several times lowering down a long PVC pipe with the minimum inner diameter that the calibration tube used by MiniCLEAN will be likely to have, 2.38 inches.

We raised and lowered the canister ten times and found that it moved smoothly during the entire distance. However, we also found that the difference in the radii of the umbilical and steel cables caused the umbilical cable to unwind too quickly, resulting in a large slack buildup that pushed against the inside of the calibration tube and prevented the canister from going down it smoothly. To fix this problem, we wound the umbilical and the steel cable together and attached them to each other using cable ties. Once we did this, we found that there was no longer any slack buildup as the cable lowered and that the cables wound and unwound from the winch drums neatly. However, when we tried to lower the canister into the tube, we found

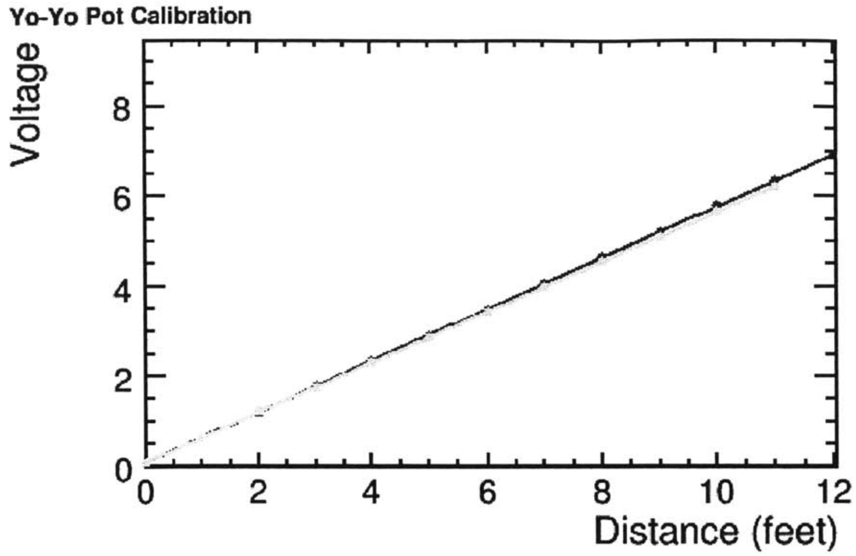

Figure 2-10: Yo-yo potentiometer output voltage (in Volts) versus cable extension (in feet). The yo-yo potentiometer calibration was done over twelve feet. The blue line is the calibration curve taken by measurements in August 2010, and the green line is the calibration curve taken by measurements in November 2010. The slope and y-intersect of this curve was used to determine absolute distances from the voltage measurements. The values for the fit parameters are given in table 2.1.

that the cable ties kept getting caught on the edge of the tube. We plan to fix this problem by binding the cables together with smooth cable sleeving.

To measure the accuracy of the deployment system, we made a set of independent measurements of the deployed distance. To do this, we tied a piece of string to the top of the canister and fed it through a loop fixed to the ground, as shown in figure 2-14. The string then ran horizontally on the ground and we measured the vertical displacement of the canister by measuring how much the string moved horizontally.

A sample of the data collected from a run is shown in figure 2-15. Each time data was recorded, the control program told the winch to lower or raise the canister six inches from its previous position. The computer would then read in the data from the yo-yo potentiometer to calculate an absolute displacement from the calibrated zero position, while the string was used to hand measure a displacement for comparison. These data show that the measurements taken by the yo-yo potentiometer are highly repeatable and that for small displacements, the yo-yo potentiometer and the string

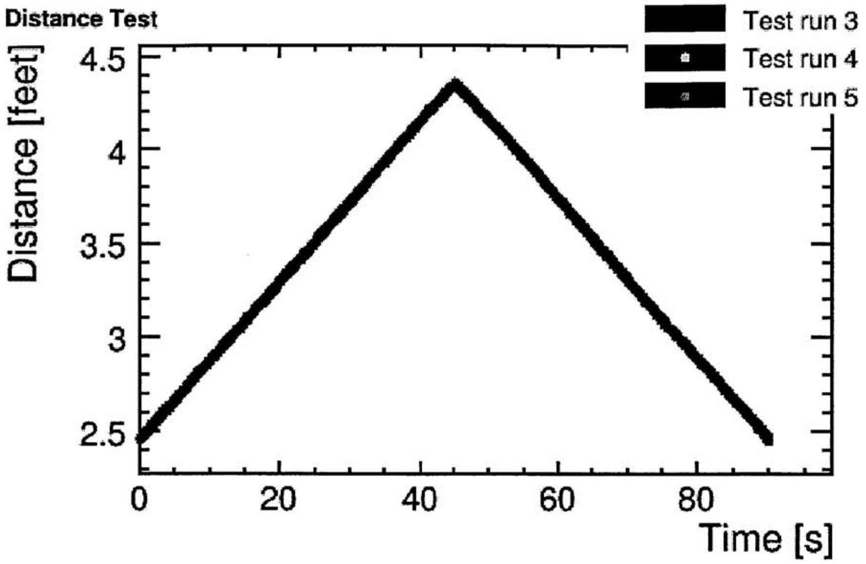

Figure 2-11: Distance measured by the yo-yo potentiometer (in feet) versus time (in seconds). Three different 90 second test runs in which the canister was lowered and then raised back up while the yo-yo potentiometer measured the distance 40 times every second. The results were so repeatable that only the results of one run are visible on the graph.

measurements agree well. However, as the winch lowers, the measurements taken by the string becomes less accurate due to moving of the string, the intrinsic measurement error (1/16") caused by measuring the string lengths by hand, and the horizontal distance between where the string connected to the ground and the part of the ground directly beneath the canister. Since the canister was free to swing in the horizontal plane, string measurements have an additional inherent error in that the length of the string may vary as the canister moves horizontally. Figure 2-16 compares the string and yo-yo potentiometer measurements to the desired error bounds of half a centimeter and shows that all of the points fall within error of the acceptable bounds.

This data, along with additional measurements taken on smaller scales are shown in figure 2-17. The computer measurements read by the yo-yo potentiometer display a Gaussian distribution with mean of 0.014 cm and RMS of 0.055 cm, while the string measurements had a mean value of 0.173 cm and an RMS of 0.321 cm and are not Gaussian distributed. While both sets of data fall well within the target precision of

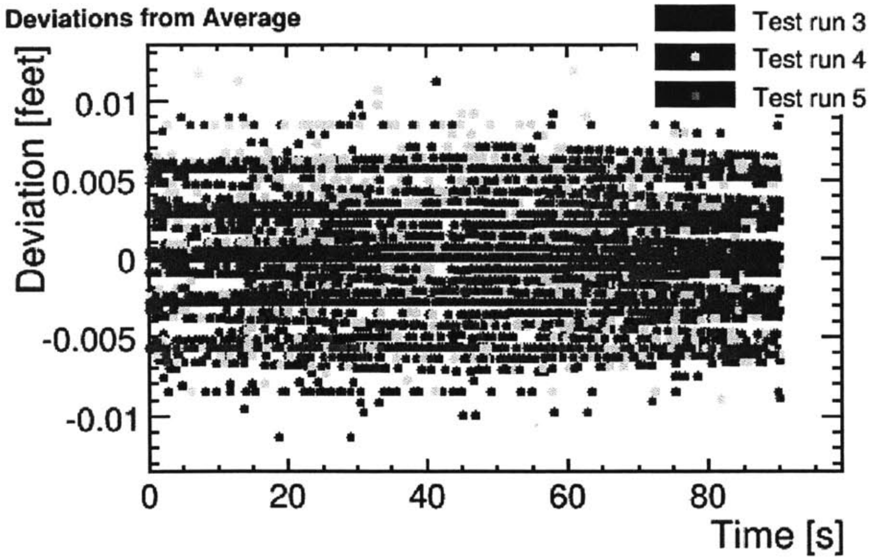

Figure 2-12: Deviation from the mean (in feet) versus time (in seconds). These graphs show the residuals from the mean of the three different 90 second measurement runs as the yo-yo pot measured the canister position 40 times every second as the canister was lowered and then raised back up. Test runs 3 had an RMS deviation of 0.0032 feet. Test runs 4 and 5 had an RMS deviation of 0.0031 feet.

0.5 cm, we claim to have a precision closer to what the computer measured, since it has less inherent error than the string measurements do. Figure 2-18 zooms in on the computer measurements to view them more closely. In this histogram, it can be seen that the errors were roughly normally distributed and well within our goal for precision.

As a final verification of the calibration of the winch controller, the computer distance measurements were plotted against the hand measurements as shown in figure 2-19. The line fit to the data shows a good agreement between the hand and computer measurements, verifying that the winch controller was accurately calibrated, that the yo-yo potentiometer is capable of measuring positions to a sufficient and repeatable accuracy, and that the entire deployment system meets the precision goal of 0.5 cm uncertainty on the canister position.

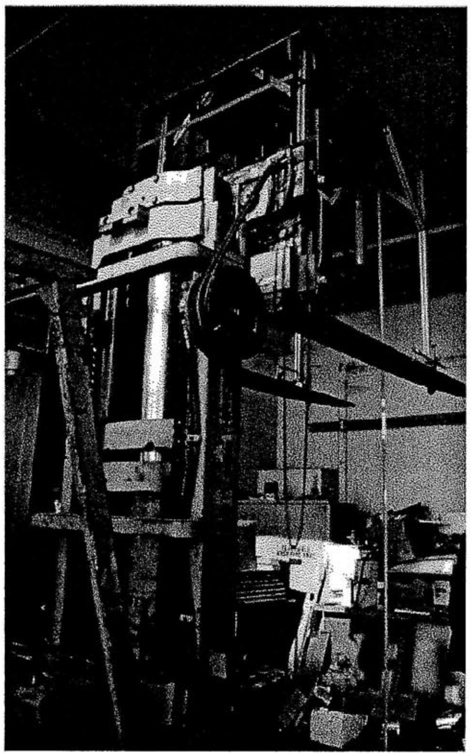

Figure 2-13: The deployment stand lifted several feet in the air during the deployment tests in the high bay.

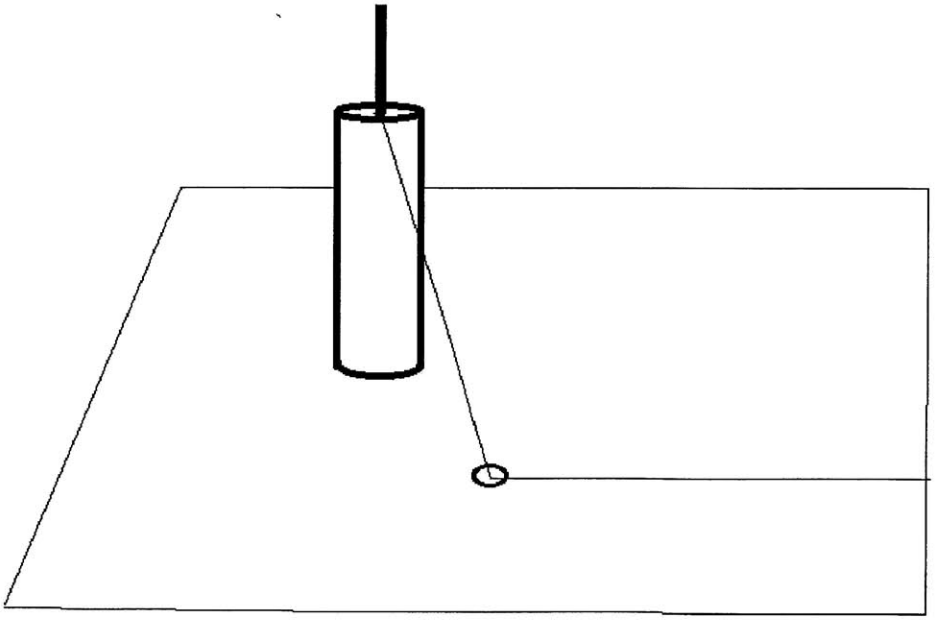

Figure 2-14: The displacement of the canister was hand-measured by tying a piece of string to the top of the canister, feeding it through a loop that was fixed to the ground, and then measuring the change in length of the string along the ground as the canister moved.

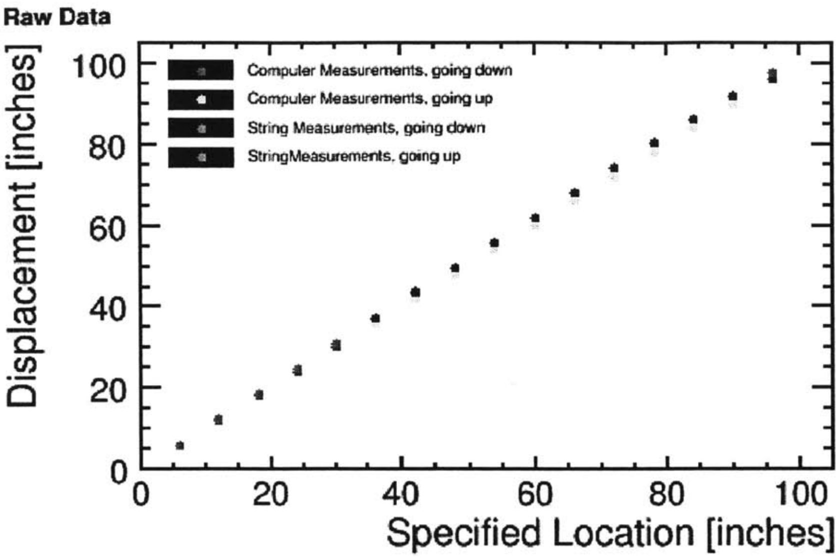

Figure 2-15: This shows the raw data measured during the tall test. Here, the displacement that the winch was told to reach is compared to the actual displacement, so the red and green points are shown as the canister was being raised and are therefore in reverse order. Note that these are displacements from the zero position, which is fully raised, so higher numbers imply that the canister is closer to the ground.

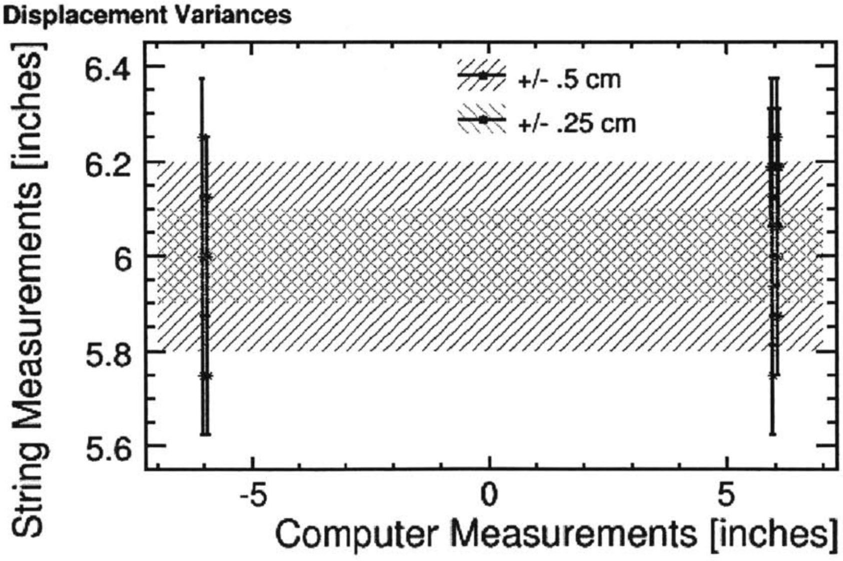

Figure 2-16: This plot shows that the yo-yo potentiometer measurements were all very close to each other and consistently near the six inch displacements that the winch was told to make. There was much more variation in the measurements taken by hand, however, since there are more measurement errors limiting the precision of the hand measurements that used the string, all of these points were still within the acceptable half centimeter error bounds

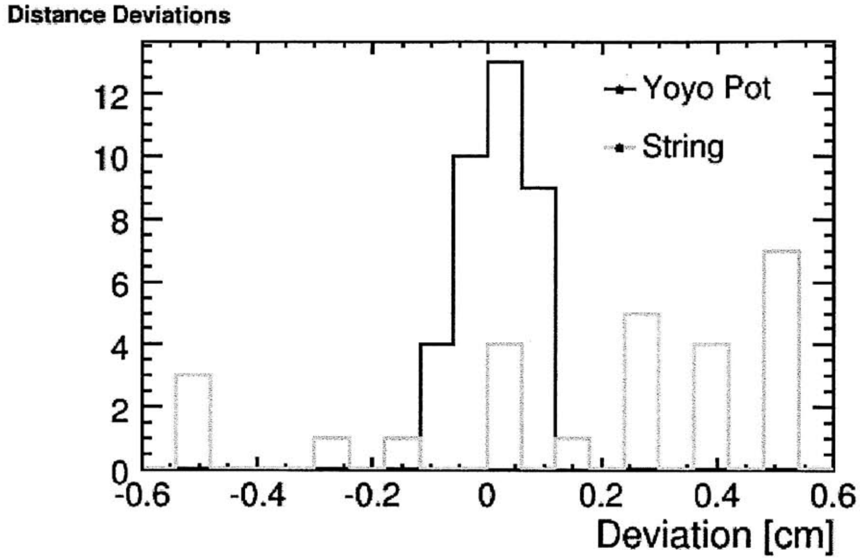

Figure 2-17: Histogram showing how far computer measured displacements and string measure displacements deviated from the specified displacements. The computer measurements show a Gaussian-shaped distribution with a mean value of 0.014 cm and RMS of 0.055 cm, while the string measurements appear to be much more crudely spread with a general trend towards over-measuring. The string measurements have a mean value of 0.173 cm and an RMS of 0.321 cm.

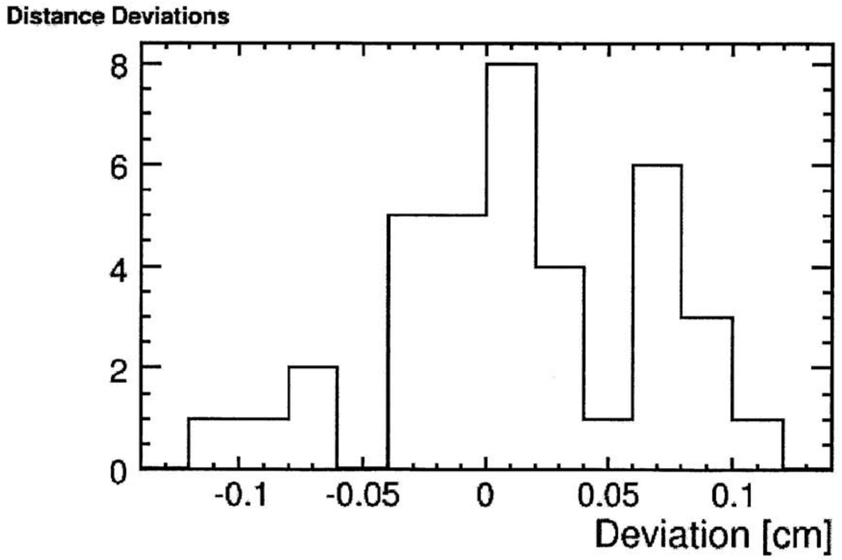

Figure 2-18: Histogram showing the same computer measurements as were shown in figure 2-17, zoomed in to better see the shape.

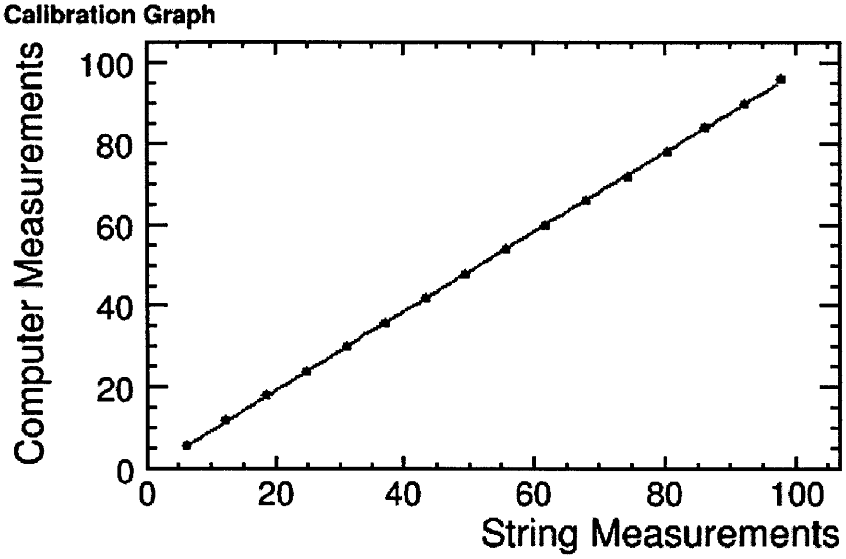

Figure 2-19: The computer measurements plotted against the hand measurements yielded a straight line with slope of 0.977±0.0088 and a y-intercept of 0, showing that the calibration reflected the actual measurements very well and that the winch controller is well-calibrated.

Chapter 3

Neutron Calibration Source

A neutron source will be used to calibrate MiniCLEAN because neutrons will form nuclear recoils with the detector nuclei and will therefore leave signals much like those left by WIMPs. By calibrating the detector with a neutron source, we can take measurements of MiniCLEAN's shielding against external neutrons while calibrating the detector's energy spectrum measurements.

3.1 Neutron Source

A Schlumberger compact neutron source called Minitron will be used to calibrate the detector response to neutrons and the efficiency of neutron background rejection cuts. A drawing of the neutron source is shown in figure 3-1.

The neutron source produces neutrons through deuterium-deuterium interactions and is referred to hereafter as a d-d source. The d-d source is a small cylinder (one inch in diameter and 5.25 inches long) full of deuteron (d_2) gas. The source contains a heating coil filament (labeled 26 in 3-1) which is coated in adsorbed deuterium particles. When the neutron source is turned on, current running through the filament heats up and causes it to release deuterium gas which is separated from the rest of the d-d source by a flange (at 7 in 3-1) and emitted at the ion source (labeled 45 in 3-1). A 2.95 V potential at 2.36 A is supplied to a cathode (at 80 and 81 in 3-1) and the cathode is heated by a heating coil (powered at 100 in 3-1). 190 V are then

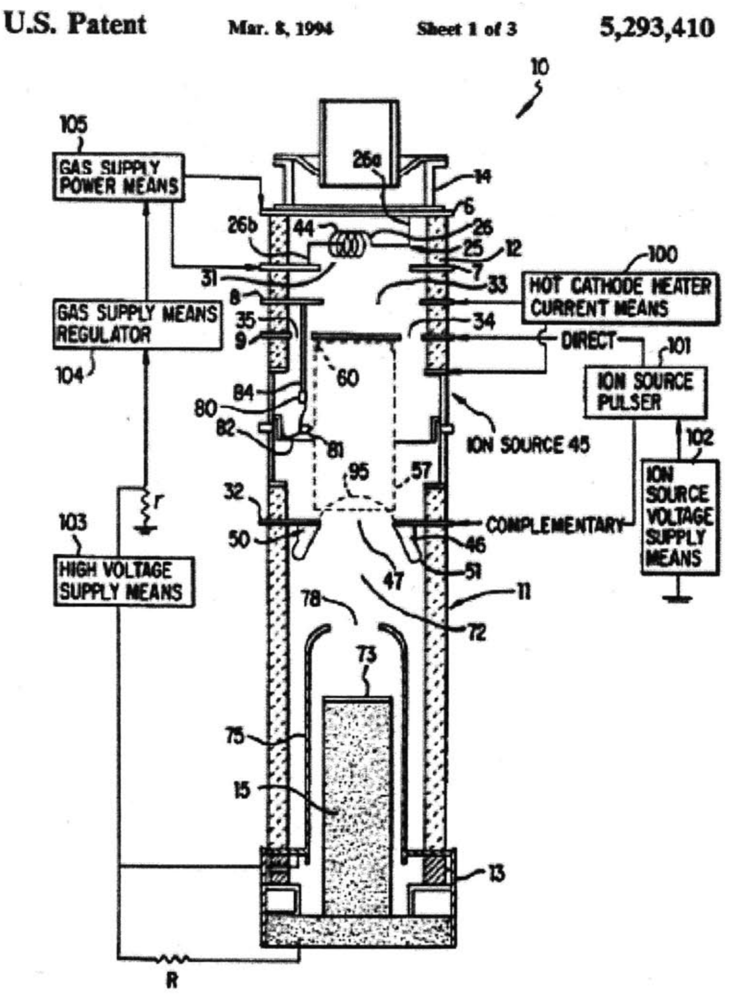

Figure 3-1: A drawing of the Schlumberger compact neutron source that we will use for calibration[2]

applied to an anode grid (labeled 57 in 3-1) that is secured to a flange (9 on 3-1) by a conductive pad (60 on 3-1). Electrons boil off of the cathode and accelerate to the anode grid, when the grid voltage is on. The electrons collide with the deuterium atoms, producing d_2 ions. These deuterium ions are accelerated across a 30 kV potential drop supplied by a high voltage source and collide with deuterium atoms adsorbed onto a tungsten target (73 on 3-1), producing fast neutrons with energy of 2.45 MeV through the reaction given in equation 3.1

$${}_1^2H +_1^2 H \rightarrow_2^3 He +_0^1 n \tag{3.1}$$

This reaction produces neutrons at a rate measured to be approximately 10^5 neutrons per second. The grid voltage can be operated in DC or pulsed mode. During calibration, the neutron source will be rapidly pulsed at a 20% duty factor with pulse length of $1\mu s$ [2]. The hardware described above is controlled by software. The final operating voltages and currents at which each part of the d-d source hardware will be held are given in table 3.1. A data table including specifications for the HV source is provided in Appendix C.

Component	Current (A)	Voltage (V)
cathode	2.36	2.95
filament	2.23	1.35
grid	25×10^{-3}	190
HV supply controller	1.99	9.44

Table 3.1: Ideal operating specifications for d-d source hardware components. The current and voltage specified for the HV supply controller are the values required to set the supply to output 30 kV[27]. These values are still tentative and the possibility of finding better operation parameters is being investigated.

3.2 Neutron Source Canister

The neutron calibration source will be deployed in a stainless steel canister. The canister consists of three parts: a top cap, a middle section, and a bottom cap.

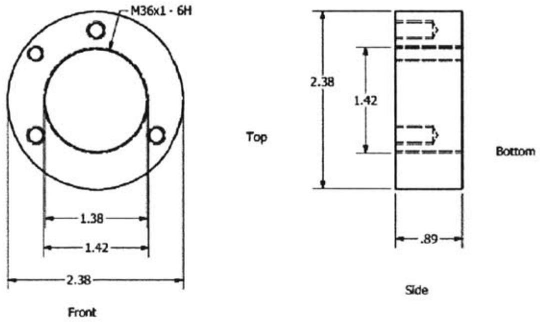

Figure 3-2: A diagram of the canister's top cap. Measurements are in inches.

Figure 3-2 shows a diagram of the top cap. A high voltage feedthrough screws into the large central threaded hole to supply power to the neutron source. The feedthrough is a GES HV Socket SB150, technical specifications are in Appendix C, and carries up to 50 kV to the neutron source. There are also four smaller screw holes. The three that are equidistant from each other have threaded eye bolts to attach to the steel cable from the deployment system. The fourth screw hole goes all the way through the top cap so that the canister can be filled with Dow Corning Compound 5 dielectric (described in Appendix D) to isolate the canister form the walls at ground from the feedthrough at 30 kV. The thermal properties of this system are discussed in Section 3.1. This hole also room for the dielectric to expand due to neutron source heating. A photograph of the top cap attached to the middle section with the feedthrough inserted is shown in figure 3-3.

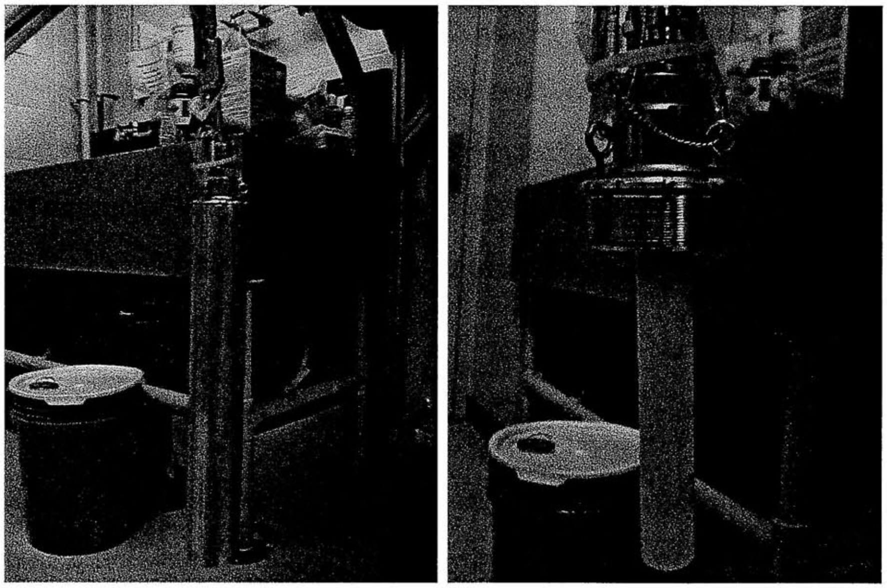

Figure 3-3: (Left) The top cap of the canister screwed into the middle section attached to the winch with the HV feedthrough installed. (Right) The top cap with the HV feedthrough inserted, attached to the winch.

Figure 3-4 shows the middle section of the canister with the holder resting at the bottom and the neutron source just above the holder. The outside of the canister is lined with twelve 0.125 inch wide and 0.062 inch deep grooves that allow wires to run along the side of the canister, in order to minimize the total outer diameter.

The acrylic holder shown in figure 3-5 sits on top of the bottom cap. The neutron source rests on the central pedestal, fitting into a groove at the tip. The two slits in the middle section allow wires to pass from the neutron source to the larger hole

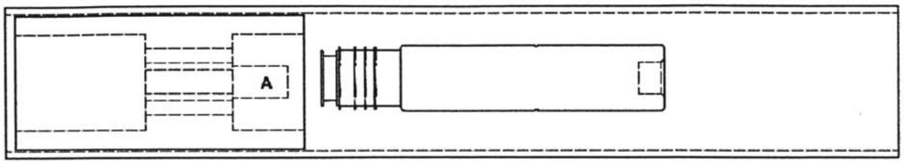

Figure 3-4: A diagram of the middle section of the canister. On the left side of the middle section is the acrylic holder; to the right of the holder is the d-d source. During operation, the d-d source will rest on the part of the holder labeled A. The d-d source is not shown resting on the holder in this picture in order to keep each part separate.

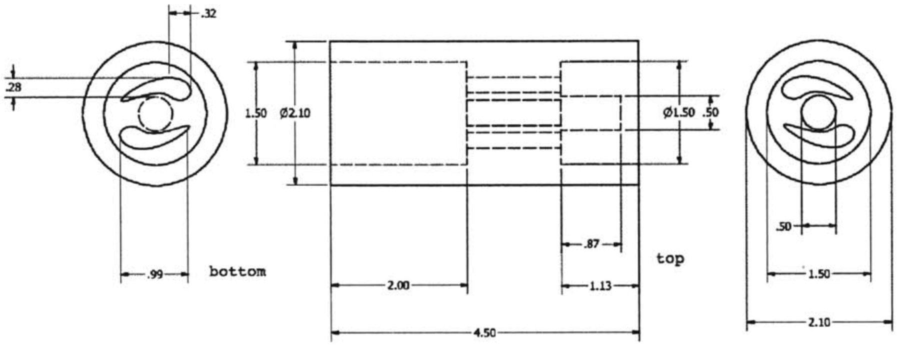

Figure 3-5: A diagram of the acrylic neutron source holder that goes inside of the middle section. Measurements are in inches.

on the bottom of the the holder, where they exit the canister through the bottom cap feedthrough. Figure 3-6 shows the neutron source resting inside the holder as it would be inside of the middle section of the canister.

The bottom cap, shown in figure 3-7, screws into the body of the middle section. The hole in the end fits a PAVE Seal Cable Harness feedthrough (part number 2189—see Appendix B for technical specifications), which allows the wires to pass through the holder to exit the canister while maintaining an airtight seal. There are 12 wires in the PAVE feedthrough, of which four are used to power the neutron source grid, filament, and cathode voltages and one is used to power the temperature sensor. Photographs of the bottom cap and the PAVE feedthrough are shown in figure 3-8.

When the canister is fully assembled, the top and bottom caps are screwed into the middle section and the high voltage and PAVE feedthroughs power and control the neutron source through an external power line, lowered by the winch with the canister. Rubber o-rings around bases of the threaded sections of the top and bottom

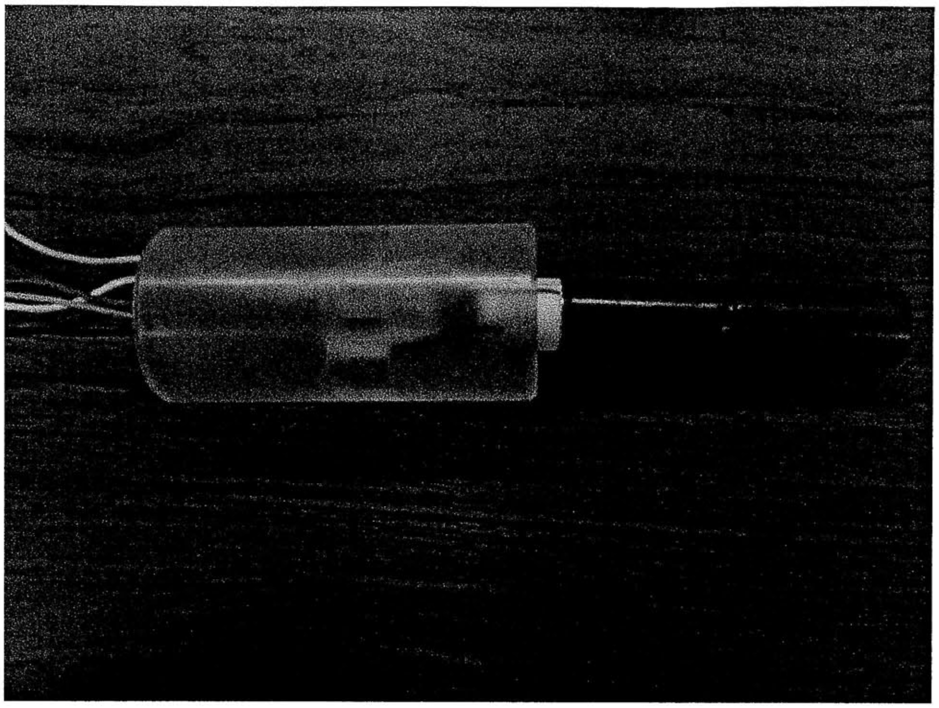

Figure 3-6: A photograph of the holder with the d-d source resting on the stand, as it would be inside of the canister.

caps keep the canister leak-tight when it is fully assembled.

3.3 Heat Generation

In order to determine how much the dielectric gel that will surround the the d-d source will expand during calibration and in order to avoid overheating the system, it is important to understand how much heat will be generated by the d-d source when

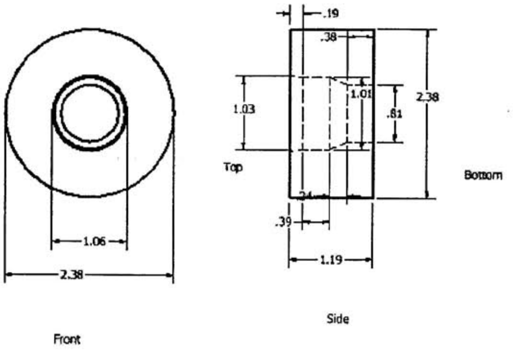

Figure 3-7: A diagram of the bottom cap of the canister

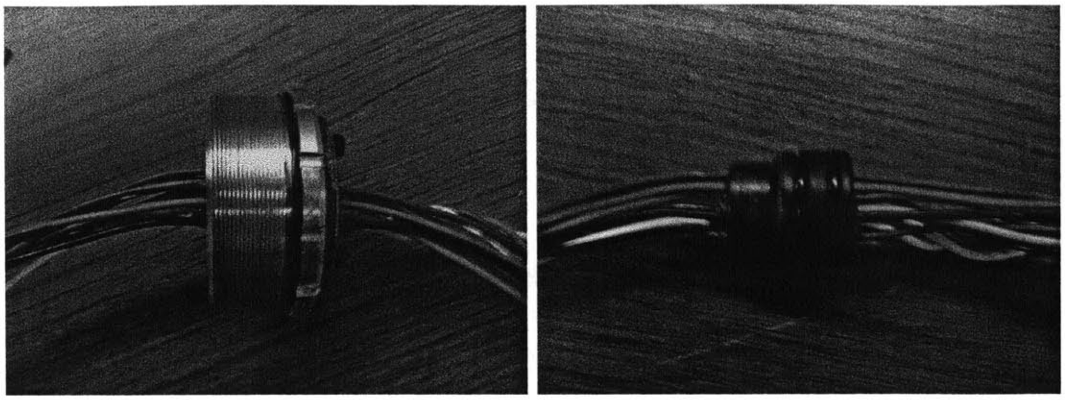

Figure 3-8: (Left) A photograph of the bottom cap with the PAVE feedthrough inserted. (Right) A photograph of the PAVE feedthrough.

it is turned on.

3.3.1 Heat Generation in Test Stand

To measure the neutron flux from the d-d source, we created a test stand that included a 3.525 inch radius hollow acrylic cylinder containing sulfur hexafluoride gas as a dielectric medium surrounding the d-d source. The d-d source was held in the center by two one inch thick semicircular acrylic stands. Figure 3-9 shows a drawing of the cross section of this setup with the conduction or convection coefficients of each material and relevant dimensions labeled. We will benchmark the final heating calculation against data from this test stand on the pressure rise in the SF_6 gas when the source is on. For this calculation we approximated that no heat would flow through the two acrylic stands, since the SF_6 is a substantially less resistive than the acrylic, and the acrylic only covers roughly one fifth of the total surface area of the d-d source.

Fourier's law tells us that the heat flux between two points is proportional to the temperature difference between them. The constant of proportionality relating the heat flux and the temperature differential is the thermal conductivity.

$$\nabla T = k\mathbf{q} \tag{3.2}$$

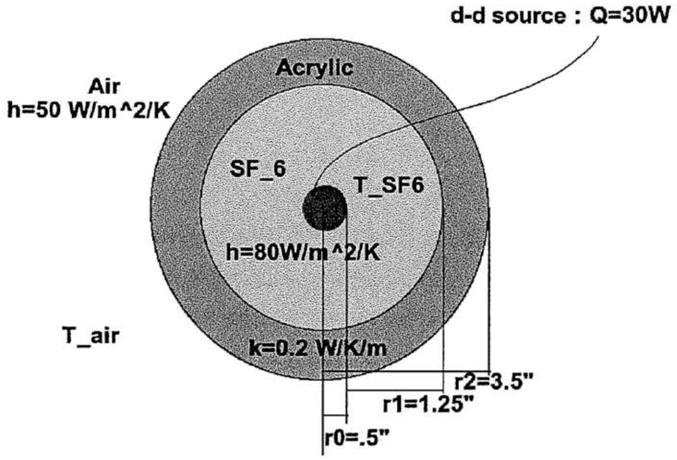

Figure 3-9: A drawing of a cross section of the d-d source test stand with relevant thermodynamic variables labeled. Within each medium, h is the convection coefficient and k is the conduction coefficient.

where T is the temperature at some point, q is the heat flux, and k is the thermal conductivity.

In a system at thermal equilibrium with no heat sources all bodies will be at the same temperature, as described by equation 3.2. However, when there is a heat source—such as the d-d source in our calibration system—we can consider the temperature differential between two points to be determined by how much each body between the two points resists the flow of heat. The resistive model of heat transfer says that the temperature difference between two points in thermal equilibrium with each other will be proportional to the heat flux and total resistance between the two points. For systems with simple geometries, such as those in which each body is a concentric cylinder, the temperature difference is described by equation 3.3.

$$\Delta T = \frac{Q}{L} R_{total} \tag{3.3}$$

where Q is the heat generated by the source per unit time, L is the length of the heat-generating body (5.25 inches for the Minitron d-d source), and R_{total} is the net resistance of the system. R_{total} is a function of each body's heat transfer coefficient and geometry.

Typically heat will flow through a solid body by conduction and through a gas by convection. Convection occurs when a gas interfaces with another body at a different temperature. If the other body is hotter than the gas, heat will flow into the gas, causing it to expand and move away from the warm body. As the gas moves away, it is replaced with cooler gas that has not yet exchanged heat with that interface. The heated gas will then cool down as it moves away from the warm body and will eventually cool down enough to return to it, creating a cycle of convection currents. When the other body is cooler than the gas, a similar process occurs. Heat flows from the gas to the cooler body, causing the gas to shrink and allowing more gas to move near the cooler body, displacing the gas that previously shrunk and creating similar convection currents.

Using a resistive heat transfer model, we can calculate the total thermal resistance between the d-d source and the air, R_{total} and find the temperature difference ΔT according to equation 3.3. The thermal resistance for conduction and convection can be calculated with the equations,

$$R_{convection} = \frac{1}{2\pi r h} \tag{3.4}$$

$$R_{conduction} = \frac{\ln\left(\frac{r_1}{r_0}\right)}{2\pi k} \tag{3.5}$$

where h is the relevant convection coefficient, k is the relevant conduction coefficient, r is the radius at which heat transfers between the media by convection, and r_0 and r_1 are the radii between which the heat conducts within a medium. The calculated thermal resistances of each part of the system are shown in table 3.2.

Material	k ($\frac{W}{m.K}$) or h ($\frac{W}{m^2K}$)	Resistance ($\frac{K.s^3}{m.kg}$)
SF_6 0[29]	$h = 80$	0.142
SF_6 1[29]	$h = 80$	0.068
Acrylic[30]	$k = 0.2$	0.891
Air[31]	$h = 50$	0.0358
Total		1.137

Table 3.2: Thermal resistances for the d-d source in the test stand. SF_6 0 and SF_6 1 are the convective resistances at r_0 and r_1, respectively.

From table 3.1, we can calculate the total heat dissipated to be 33.5 W in DC mode. Since we are pulsing the d-d source with a 20% duty cycle, the HV supply controller is only on for one fifth of the time while the rest of the electronics are on the entire time. Calculating the power P generated by the electronics where each component has current I and voltage V, $P = IV$, we find that there is a total of 18.5 W generated by the neutron source while it is in pulse mode. This calculation of the heat generation involves using the time average of the heat generated by the neutron source. Our calculation of the change in temperature will therefore be an approximation, since it neglects the differences in heat flow through the test stand system when the HV supply controller is on and off by assuming that the heat generation is constant. Using this approximation, we calculate the total change in temperature to be 158 K at thermal equilibrium. Assuming that the system starts out at room temperature $T_{air} = 298$ K, we calculate the final temperature of the SF_6 to be 456 K.

By assuming that the SF_6 can be modeled as an ideal gas and measuring the pressure change within the test stand, we can test this prediction. The measured an increase in pressure is a factor of 1.45 after the d-d source was on for 5 hours. The calculated temperature change above predicts a change in pressure by a factor of 1.54. This calculated fractional increase is greater than the measured fractional increase by 6%. This error is likely due to the approximation made when using the time average of the power generated.

3.3.2 Heat Generation in MiniCLEAN

We use a similar resistive heat model to calculate the change of temperature in the dielectric gel surrounding the d-d source during the calibration of MiniCLEAN. The calibration system consists of a stainless steel tube that runs through the water tank and into the vacuum inside the outer vessel. Since the volume of the water is much greater than the size of the tube, the water will remain at a constant temperature throughout the process. Additionally, the water bath around the tube will allow all of the heat that flows through the tube to convect into the water. We therefore ignore the vacuum inside of the outer vessel for this calculation and consider only the heat that leaves the tube via convection with the water. Figure 3-10 shows a drawing of the cross section of the d-d source in the canister with the dielectric gel in a steel tube surrounded by water.

Table 3.3 shows the relevant conduction coefficients and resistances for this system.

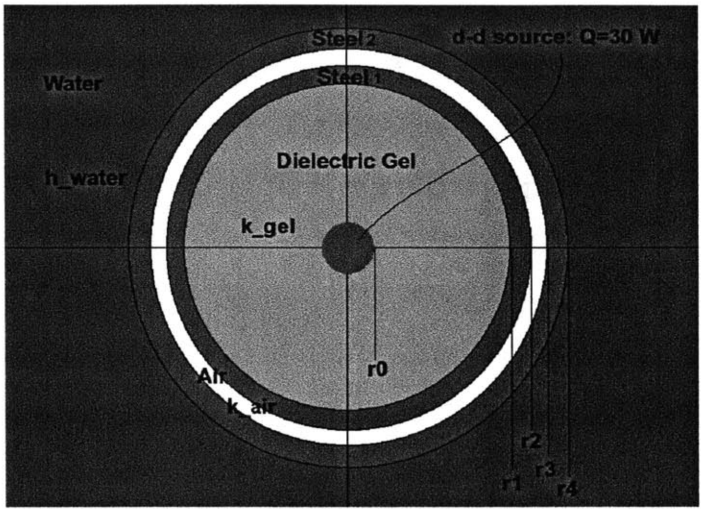

Figure 3-10: A cross section drawing of the d-d source surrounded by the dielectric gel inside the steel canister in the calibration tube surrounded by water. $r_0 = 0.55$ inches, $r_1 = 1.078$ inches, $r_2 = 1.191$ inches, $r_3 = 1.334$ inches, and $r_4 = 1.490$ inches.

Material	k ($\frac{W}{m.K}$) or h ($\frac{W}{m^2K}$)	Resistance ($\frac{K.s^3}{m.kg}$)
Dielectric Gel[32]	$k = 0.25 \pm 0.13$	$0.428^{+0.429}_{-0.142}$
Steel 1[1]	$k = 54$	2.94×10^{-4}
Air 1[31]	$h = 50$	0.105
Air 2[31]	$h = 50$	0.094
Steel 2[1]	$k = 54$	3.26×10^{-4}
Water	$h = 60$	0.0701
Total		$0.699^{+0.429}_{-0.142}$

Table 3.3: Thermal resistances for the d-d source during calibration. Steel 1 is the resistance at innermost steel cylinder, and steel 2 is at the outermost one. Air 1 and air 2 are the resistances of the air at r_2 and r_3, respectively.

Using the average heat generation of 18.5 W, as before, and using the calculated total resistance and d-d source length of 5.25 inches, equation 3.3 implies that the dielectric gel will increase in temperature by $92.6^{+56.8}_{-18.8}$ K once the system reaches equilibrium. Since the water will be held near 303 K and we expect the entire system to be at thermal equilibrium with the water before the calibration begins, the final temperature of the dielectric gel will be approximately $395.6^{+56.8}_{-18.8}$ Kelvin. Uncertainties in this calculation come from the uncertainty in the conduction coefficient of the dielectric gel. Since the d-d source will only ever be running for 1005 seconds (as calculated in Chapter 4), we do not expect the system to come to thermal equilibrium, so we expect this temperature change to be an overestimate of what the gel will actually experience. We also expect this equilibrium temperature to be approximately 6% greater than the actual equilibrium temperature due to the approximation made in averaging over the power generation.

Dielectric Gel Expansion

The dielectric gel (Appendix D lists relevant specifications) has a coefficient of thermal expansion of $\alpha = 7 \times 10^{-4}\ \mathrm{K}^{-1}$[8]. Using the relation,

$$\Delta V = V_0(e^{\alpha \Delta T} - 1) \tag{3.6}$$

(where ΔV is the change in the gel's volume, ΔT is the change in temperature, and V_0 is the initial volume of the gel) and the fact that the initial volume of the dielectric gel is approximately 526.5 mL, we find that the change in volume is $35.3^{+22.7}_{-7.4}$ mL . Since the gel is constrained to expand along the long axis of the canister cylinder, we find that the gel expands to be $1.50^{+0.96}_{-0.32}$ cm higher than it previously was.

When filling the canister with dielectric gel, up to $1.50^{+0.96}_{-0.32}$ cm should be left between the top of the gel and the top of the canister for clearance for the gel to expand.

Chapter 4

Calibration Simulations

In order to study the calibration system and process, we used GEANT4 to simulate the MiniCLEAN calibration system and detector geometry. We used these simulations to determine the impact of the calibration tube on the neutron background and to study how the calibration neutron signal and required calibration time is affected by the calibration system.

4.1 Calibration System Background

4.1.1 Neutron Background Sources

To understand the effects of the calibration system on the neutron background, we first study the sources of the neutron background in the detector environment. Once we establish what the background is, we simulate the detector geometry with and without the calibration tube filled with air to obesrve the change in measured background neutron spectrum.

Muon-Induced Neutrons

While going deep underground allows MiniCLEAN to avoid most cosmic ray radiation, the muons that are stopped by the earth can undergo spallation and produce fast neutrons and radioisotopes [39]. While both of these are sources of background, the fast neutrons are particularly difficult to shield against and can produce nuclear recoils in the energy range of interest to MiniCLEAN.

In order to assess the muon-induced neutron production rate, it is first important to assess the muon flux on a given site. [17] presents a model of cosmic muon depth versus intensity relationship as

$$I(x) = I_1 \exp^{-x/\lambda_1} + I_2 \exp^{-x/\lambda_2} \tag{4.1}$$

Here, I_1, I_2, λ_1, and λ_2 are free parameters and x is the depth. This relationship shows how the muon intensity decreases the farther one goes underground, and so deeper sites have less muon-related backgrounds to account for.

Using this equation and experimental data, including data taken directly at specific sites and data recorded at regular depths underground, [39] fit the parameters and found that the model fits the data well, with $I_1 = 67.97\text{cm}^{-2}\text{s}^{-1}$, $I_2 = 2.071\text{cm}^{-2}\text{s}^{-1}$, $\lambda_1 = 0.285$ k.w.e, $\lambda_2 = 0.698$ k.w.e. Figure 4-1 shows the results. The depth in this graph is in units of kilometers of water equivalent (k.w.e.); since overburden materials have different densities and neutron interaction cross sections, these units normalize for the material the neutrons are passing through between different sites by equating the distance under rock to an equivalent distance under water. As the graph shows, SNO Lab, in Sudbury, has a muon flux of $(3.77\pm0.41) \times 10^{-10}\text{cm}^{-2}\text{s}^{-1}$ at a depth of

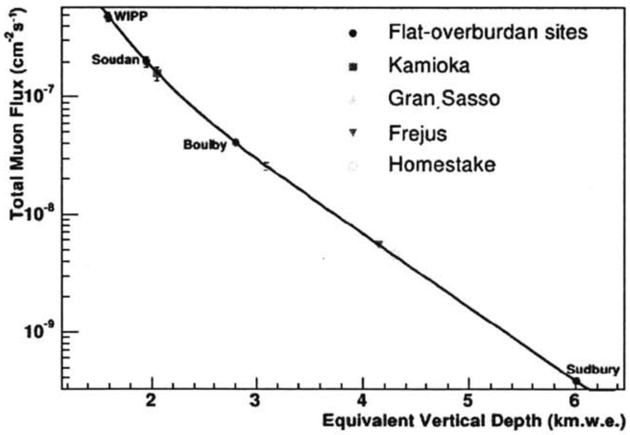

Figure 4-1: Graph from [39] showing the muon intensity at various sites of interest to dark matter and neutrino experiments. Fitted to the data is equation 4.1

6.011 ± 0.1 km of water equivalent; for comparison, the muon flux at the surface is $70.04\ \mathrm{cm}^{-2}\mathrm{s}^{-1}$.

The muon-induced neutron production rate varies depending on the material that the muon is passing through, and so the chemical composition of the rock around the detector plays a key role in determining the neutron flux. In general, due to the $\frac{Z^2}{A}$ electromagnetic cross section dependence, [39] has found through FLUKA simulation that the average number of neutrons, $< n >$, produced by a muon, accounting for resulting electromagnetic showers, is

$$< n >= 1.27 \times 10^{-4} \left(\frac{Z^2}{A}\right)^{0.92} n/(\mu\mathrm{g} \cdot \mathrm{cm}^{-2}) \tag{4.2}$$

where Z is the atomic number of a given nucleus, and A is the nucleus's atomic mass number. Holding material constant, [39] models the neutron flux versus depth relationship as

$$\phi_n = P_0 \left(\frac{P_1}{h_0}\right) \exp^{-h_0/P_1} \tag{4.3}$$

Here, ϕ_n is the neutron flux, P_0 (experimentally found to be $(4.0\pm1.1)\times10^{-7}\ \mathrm{cm}^{-2}\mathrm{s}^{-1}$) and P_1 (experimentally found to be 0.86 ± 0.05 km of water equivalent) are parameters that were fit to the measured flux at various depths, and h_0 is the vertical depth of the site in kilometers of water equivalent. Equation 4.3 accounts for higher multiplicity interactions where a single muon leads to the production of multiple neutrons. The data that these parameters fit come from measurements taken of the neutron flux at several sites, shown in figure 4-2.

Reference [39] predicts a total muon-induced neutron flux of $11 \times 10^{-12}\mathrm{cm}^{-2}\mathrm{s}^{-1}$ for neutrons with energies below 1 MeV that may be a background to MiniCLEAN's signal.

(α,n)-Induced Neutrons

A disadvantage to being deep underground is the presence of heavy nuclei. In particular, rocks within the earth are rich in α particle emitters such as elements in the decay chains of uranium and thorium. While α particles are easily shielded against,

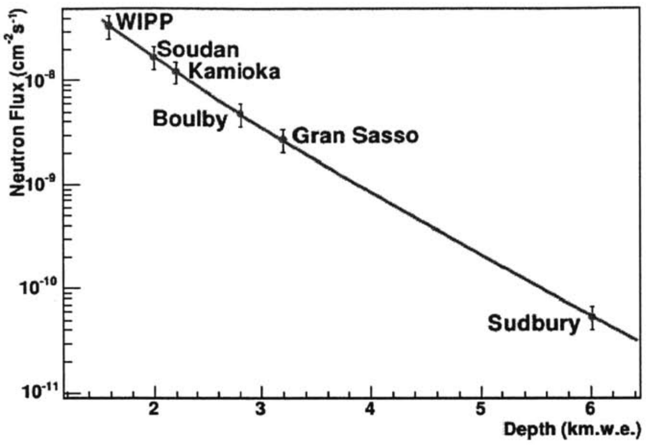

Figure 4-2: Graph from [39] showing the muon-induced neutron flux measured at several sites with equation 4.3 fit to the data. The error bars on the points come from the uncertainty of the measurements of the muon and neutron flux at each location.

the secondary effects of their interactions may produce backgrounds that must be accounted for. When an α particle is created by a uranium or thorium decay, the alpha may then collide with another nearby nucleus and free a neutron, which will then provide additional background to the detector. In addition to being generated by the surrounding rocks, α particles may come from internal detector components, such as photomultiplier tubes whose glass windows contain uranium and thorium. Further α contamination can come from ambient radon depositing its long-lived α-emitting daughters on sensitive detector components.

In general, (α,n) neutrons dominate the neutron flux around the detector by two to three orders of magnitude due the abundance of these α emitters. This was shown in [39], as seen by figure 4-3. As the figure shows, the (α,n) neutron yield in the case where only the rock cavern cavity is used for shielding is roughly three orders of magnitude greater than muon-induced interactions. Reference [15] shows that the neutron yield (Y) of a given element is

$$Y = \frac{N_A}{A} \int_0^{E_0} \frac{\sigma(E)}{S(E)} dE \tag{4.4}$$

where N_A is Avogadro's number, A is the atomic mass number of the element, σ is

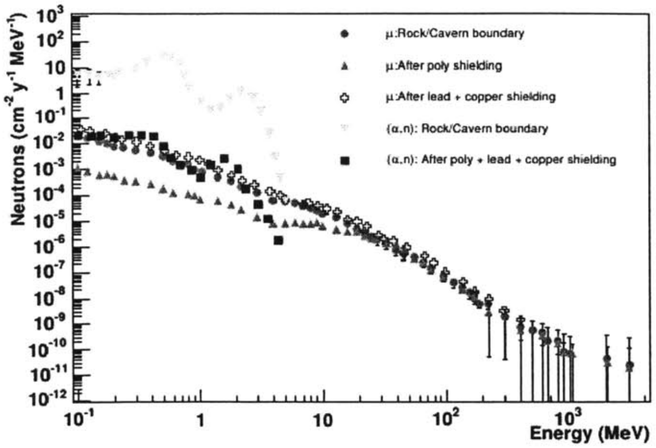

Figure 4-3: Graph from [39], showing neutron energy spectrum for fast neutrons produced by muon-induced interactions and (α,n) interactions in rock. This graph shows the neutron yields of both types of radiation with and without shielding and shows that the (α,n) neutron flux with a rock cavern boundary in the energy range of interest — around 0.1 MeV — is approximately three orders of magnitude greater than the muon induced neutron flux.

the interaction cross section for an α particle with that element at a given energy, E_0 is the initial energy, and S is the mass stopping power of the element. To find the total neutron yield from a given element, [15] assumes that the incident α flux with energy E_j is constant until it is fully attenuated and expands this equation to

$$Y(E_n) = \frac{N_A}{A} \sum_j \frac{R_\alpha(E_j)}{S(E_j)} \int_0^{E_j} \frac{d\sigma(E_\alpha, E_n)}{dE_\alpha} dE_\alpha \tag{4.5}$$

where E_n is the neutron energy, E_j is the specific energy of the α particles, and R_α is the α particle production rate for the element, given by

$$R_\alpha(E_n) = 10^{-6} \frac{N_A}{A_\alpha} \frac{\ln 2}{t_{1/2}} B_j \tag{4.6}$$

where $t_{1/2}$ is the half life of the decay and B_j the branching ratio of the decay with energy E_j.

Since MiniCLEAN uses liquid argon, the (α,n) neutron flux for α interactions in argon is of particular interest. Figure 4-4 shows the neutron kinetic energy distribution predicted from both uranium and thorium sources.

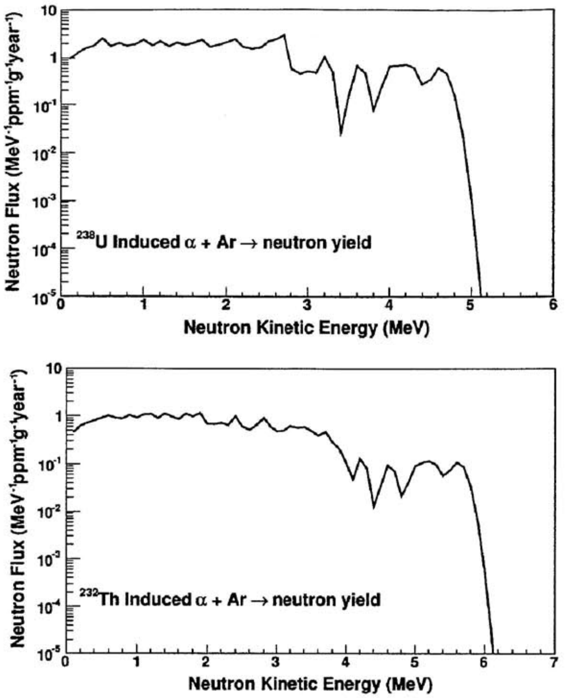

Figure 4-4: Neutron flux (in Mev^{-1}ppm^{-1}g^{-1}year^{-1}) versus neutron kinetic energy (in MeV). The (α,n) neutron energy spectrum in argon, calculated by [15].

4.1.2 Neutron Background Simulations

We simulated the geometry of detector and its environment in GEANT4 and used the neutron spectra as described above to generate and track neutrons moving through the detector. To study the effects of the calibration system on the background rates, we simulated the background over two different geometries: the plain detector geometry, and the same detector geometry with a calibration tube filled with air installed. We simulated 887200 neutrons for the geometry without the calibration tube and 538300 neutrons for the geometry with the tube. Figure 4-5 shows the deposited energy spectrum for neutrons interacting within the fiducial radius for the detector geometry with no tube. After running the simulation, we find that the number of neutrons that interacted within the energy region of interest between 20 and 100 keVee—the recoil energy range that will provide the most background—corresponds to an interaction rate of 0.0638 neutron-nucleon scatters per year. Figure 4-6 shows the deposited energy spectrum for neutrons interacting within the fiducial radius for the detector

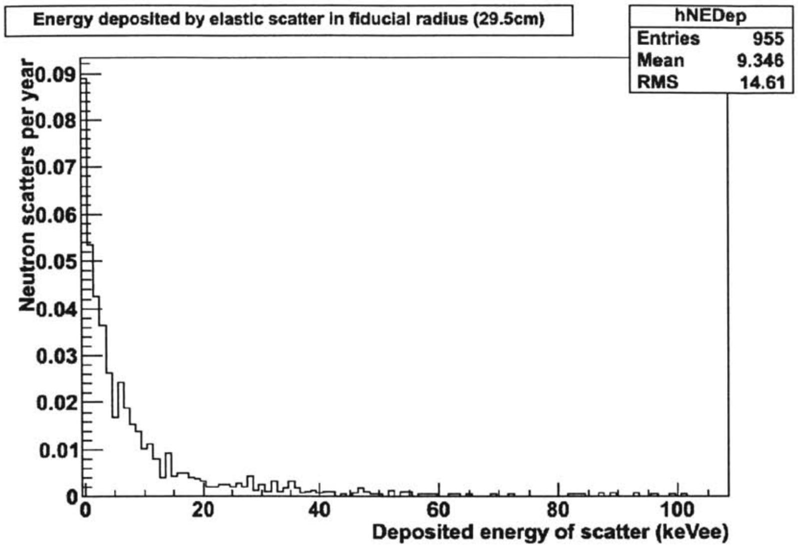

Figure 4-5: Number of neutron scatters per year versus recoil energy (in keVee). This graph shows the energy distributions for neutrons that interacted within the fiducial radius for the MiniCLEAN geometry with no calibration tube. The simulation showed a total of 0.0638 scatters per year between 20–100 keVee.

geometry with the calibration tube filled with air installed. The simulation resulted in an event rate of 0.0676 scatters per year for neutrons interacting within the fiducial radius and depositing between 20 and 100 keVee.

This slight increase in external neutron background rate is within the statistical error of the simulation, so we conclude that the air-filled calibration tube does not increase the external neutron background.

4.2 Calibration System Signal

We simulated the neutron source as an isotropic neutron-emitter, located in the center of the canister, positioned near the bottom of the calibration tube. We ran separate simulations of the neutron source, each producing 9×10^5 neutrons at 2.4 MeV. These simulations were run once for each of three different geometries.

The first geometry is the standard one and consists of the MiniCLEAN detector without the tube and canister present, only an isotropic neutron source located adjacent to the photomultiplier tubes at a radius of 105.41 cm from the center of

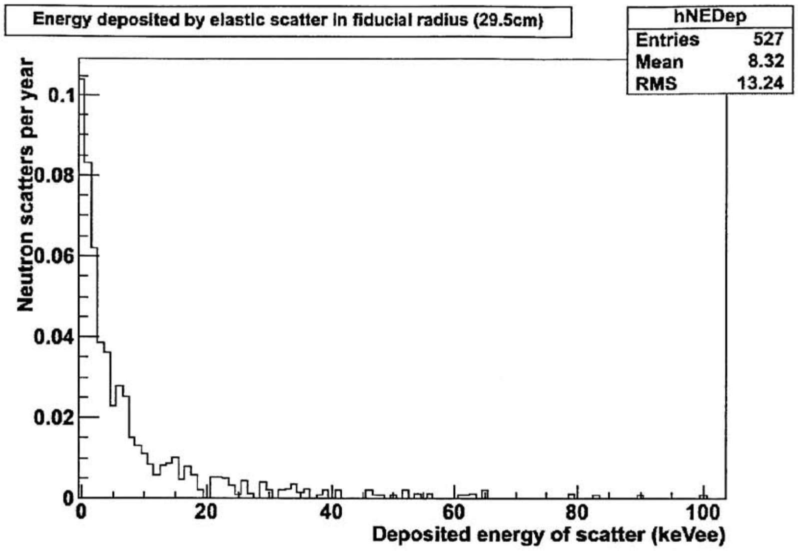

Figure 4-6: Number of neutron scatters per year versus recoil energy (in keVee). This graph shows the energy distributions for neutrons that interacted within the fiducial radius for the MiniCLEAN geometry with the calibration tube. The simulation showed a total of 0.0676 scatters per year between 20–100 keVee.

the detector. The second geometry is the same as the first, but with the addition of a steel calibration tube containing the neutron source, and the third geometry additionally contains the canister, dielectric gel, and acrylic holder. Figure 4-7 shows a simple picture of MiniCLEAN's inner vessel surrounded by photomultiplier tubes (red). The gray cylinder running tangent alongside the photomultiplier tubes is the calibration tube, and the green cylinder near the bottom of that is the canister and its contents. The d-d source is located at the center of the canister. The rest of the MiniCLEAN geometry and environment, while present for the simulation, was made invisible in figure 4-7 for simplicity.

For these simulations, we care most about the neutron-induced argon recoils that deposit energies between 12.5 keVee and 25 keVee. This energy window is referred to as the region of interest, and is the region where we most expect neutron events to look like WIMP events. We also limit the volume of liquid argon in which we accept events in order to eliminate external α backgrounds; the fiducial radius is 29.5 cm.

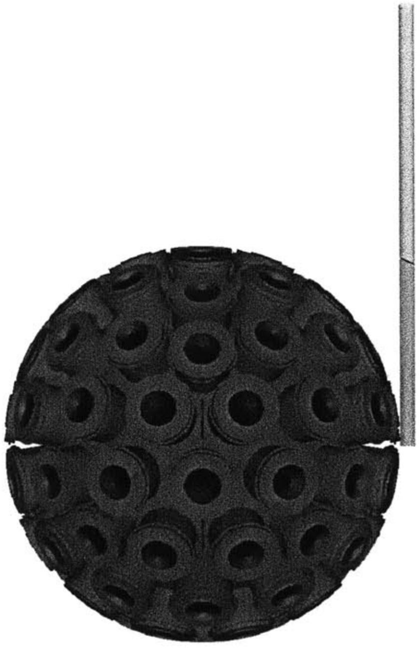

Figure 4-7: A simple drawing of the inside of MiniCLEAN with the full calibration system installed. Note that the line separating the two halves of calibration tube is an artifact marking where the tube intersects the outer vessel and is not actually a hole in the geometry.

4.2.1 Standard Geometry Results

We simulated 9×10^5 neutrons isotropically emitted at 2.4 MeV kinetic energy at a radius of 105.41 cm and height of 20.46 cm, the center of where the calibration tube would be if it existed in this geometry.

With the simulation output, we study the distances of closest approach for each of the generated neutrons to see which parts of the detector they interacted with. Figure 4-8 shows this, with the outer vessel wall, photomultiplier tubes, acrylic shield, wavelength shifter, and fiducial volume labeled. Note that the fiducial volume and the regions with radius less than the photomultiplier tubes, excluding the acrylic region, are all filled with liquid argon. The large decrease in event number by the fiducial volume indicates effective self shielding, as only 0.0092 of the neutrons that interact with the detector make it into the fiducial volume.

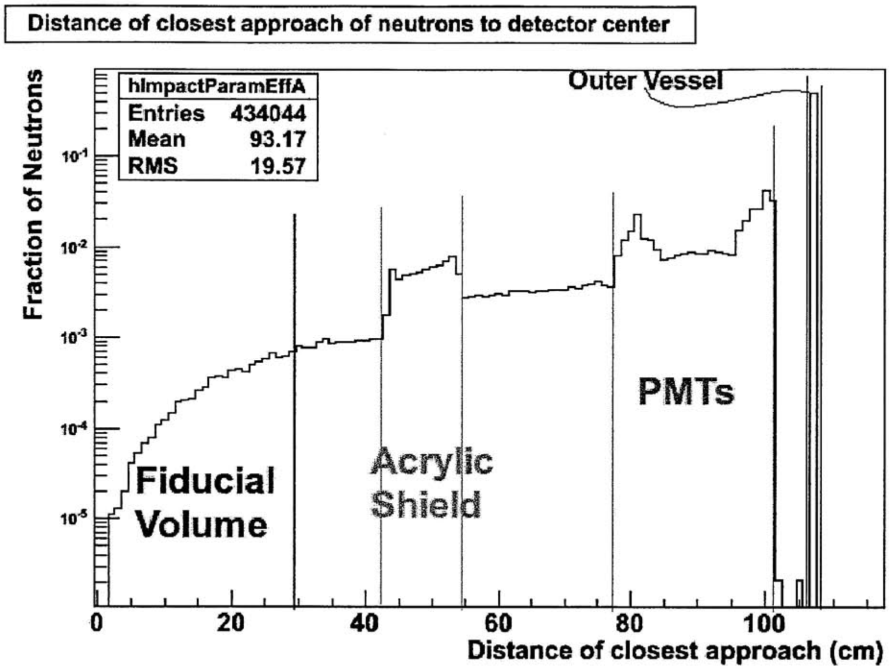

Figure 4-8: Fraction of total neutron reactions versus distance of closest approach (in cm). The spatial distribution of neutron interactions as they passed from the d-d source to the center of the detector for the standard geometry. The histogram bins how many interactions occurred at each distance from the center of the detector. Features on the histogram are labeled with which parts of the detector they occur at, including the outer vessel wall, the photomultiplier tubes, the wavelength shifter, and the fiducial volume. Note that the unlabeled regions between the photomultiplier tubes and fiducial volume are all filled with liquid argon.

The neutron-induced nuclear recoil deposited energy, for interactions that occur within the fiducial volume, is shown in figure 4-9. Since each neutron interaction is independent, we can model whether or not we observe such an event as a Poisson process. Additionally, because we have simulated a large number of neutrons and we know that the energy deposition distribution around the region of interest looks approximately exponential, we can treat the number of neutrons that interact within the desired energy region of interest as a Gaussian-distributed variable with mean $\mu = NP_i$ and standard deviation $\sigma = \sqrt{NP_i}$, where N is the number of neutrons produced by the d-d source and P_i is the probability of a neutron interacting within a specified region. For a Gaussian distribution with 5% errors, we say that $0.05\mu = \sigma$. Using μ and σ as defined above, we find that $N = \frac{400}{P_i}$.

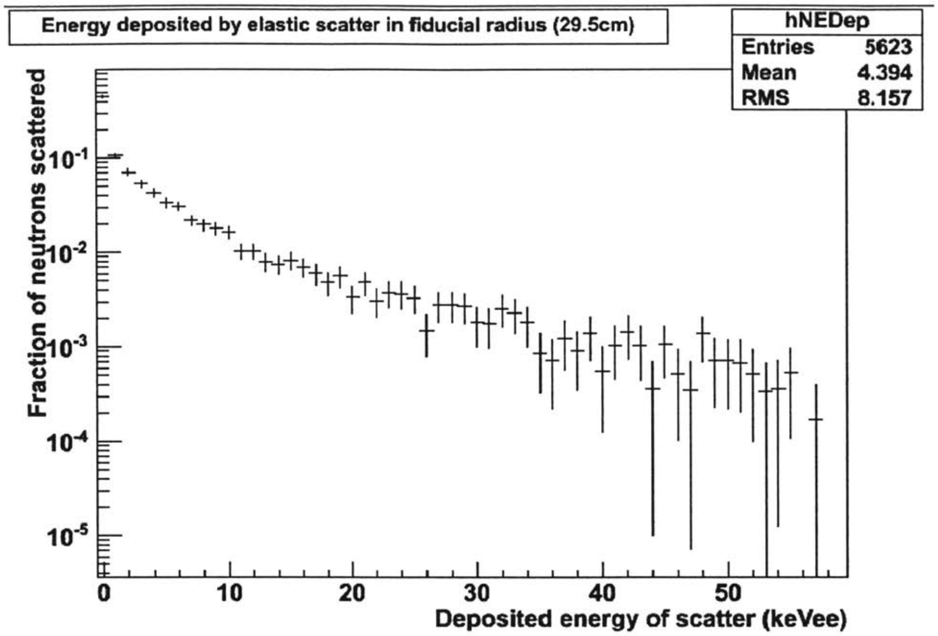

Figure 4-9: Fraction of neutron interactions within fiducial volume versus recoil energy (in keVee). The normalized neutron deposition energy distribution within the fiducial volume for the standard geometry with no calibration system.

There are two different probabilities P_i that are interesting: (1) the number of neutrons needed to have 5% statistical uncertainty on the total number of neutrons that interacted in the fiducial volume within the energy region of interest, and (2) and the number of neutrons needed for each energy bin in the energy region of interest, interacting in the fiducial volume, to have 5% statistical uncertainty. We consider the energy in 2 keVee bins, corresponding to ten times the energy resolution of the detector. In order to determine the number of neutrons needed for each bin in the region of interest to have 5% statistical uncertainty, we consider, out of all events, the proportion, P_2, that interacted within the fiducial volume within the highest energy bin, 23 to 25 keVee. This energy bin is chosen because it is expected to have the fewest events out of all of the bins in the region of interest. To determine the number of neutrons needed to have 5% statistical uncertainty on the total number of neutron interactions within the region of interest in the fiducial volume, we consider the proportion of events, P_1 that interacted between 12.5 and 25 keVee in the simulations.

Extracting these two numbers from the simulation, we find that $P_1 = 2.62 \times 10^{-4}$

and that $P_2 = 3.53 \times 10^{-5}$. Values for P_1 and P_2 can be seen in table 4.1. During the actual calibration, the neutron source will be run in a pulsed mode with 1 microsecond pulses and a 20% duty cycle, meaning that neutrons will be produced for one fifth of the total calibration time. The corresponding required total number of neutrons and calibration times are in table 4.2.

4.2.2 Geometry with Calibration Tube Results

We simulated 9×10^5 neutrons with the calibration tube in place. Figure 4-10 shows the spatial distribution of the neutron reactions throughout MiniCLEAN. The addition of the calibration tube is visible between the outer vessel wall and the photomultiplier tubes where the slope drops off, rather than the steep cutoff we saw in figure

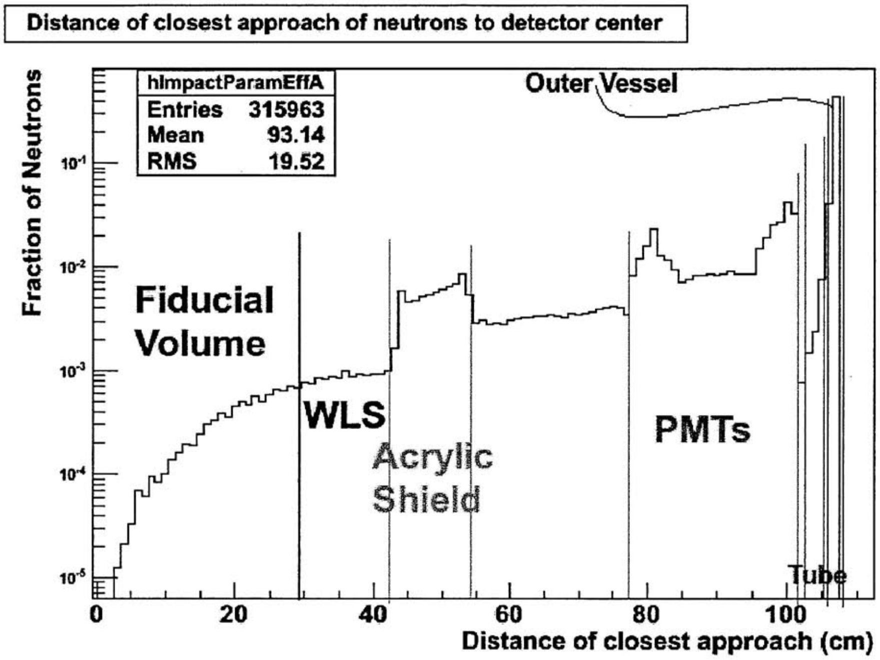

Figure 4-10: Fraction of total neutron reactions versus distance of closest approach (in cm). The spatial distribution of neutron interactions as they passed from the d-d source to the center of the detector. The histogram bins how many interactions occurred at each distance from the center of the detector for the standard calibration geometry with an added tube. Features on the histogram are labeled with which parts of the detector they occur at, including the outer vessel wall, the calibration tube, the photomultiplier tubes, the acrylic shields, the wavelength shifters, and the fiducial volume. Note that the unlabeled regions between the photomultiplier tubes and fiducial volume are all filled with liquid argon.

4-8.

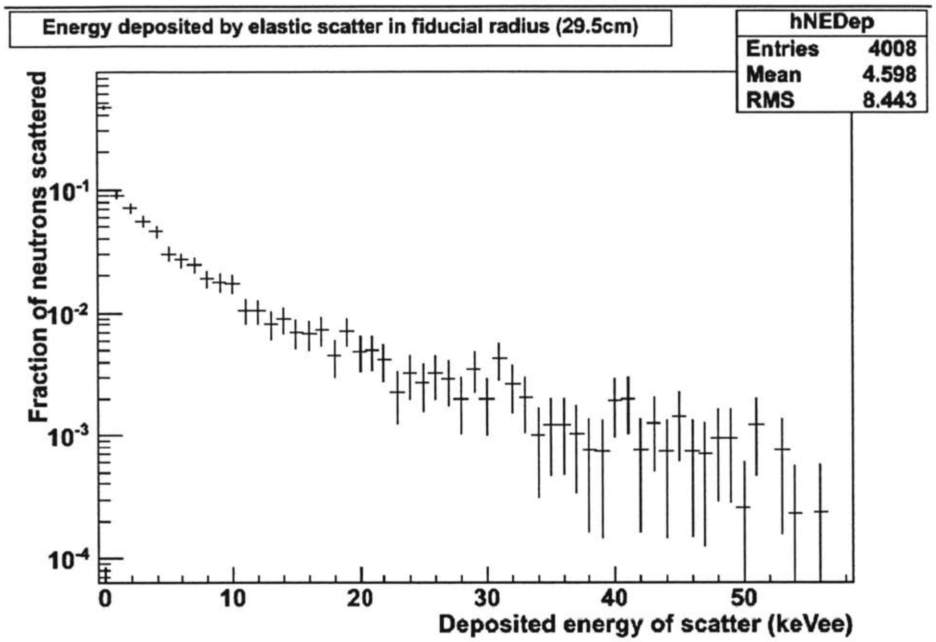

Figure 4-11: Fraction of neutron interactions within fiducial volume versus recoil energy (in keVee). The normalized deposited energy distribution from neutron interactions within the fiducial volume for the standard geometry with the calibration tube.

Similarly, we can determine the values of P_1 and P_2 for 5% statistical uncertainty in this geometry by examining the energy distribution within the fiducial volume, shown in figure 4-11. By considering the fraction of total neutrons that interact within the fiducial volume within the energy region of interest and the last bin of the region of interest, we find $P_1 = 1.93 \times 10^{-4}$ and $P_2 = 1.94 \times 10^{-5}$. Values for P_1 and P_2 are summarized in table 4.1. Calculating the minimum number of neutrons needed for 5% measurements and the time it will take to produce them results in the values in table 4.2. These times are approximately two times longer than those calculated for the standard geometry, showing that the calibration tube blocks approximately half of the neutrons and extends the required calibration time.

4.2.3 Full Calibration Geometry Results

After simulating 9×10^5 neutrons in the full calibration geometry—including the steel calibration tube, the dielectric gel, the steel canister, and the acrylic holder—we were able to study the distribution of neutrons that interact within the region of interest within the fiducial volume. Figure 4-12 shows the neutron interaction impact parameter distribution. Figure 4-13 shows the energy deposition distribution for neutron interactions that occur within the fiducial volume. We measure $P_1 = 1.611 \times 10^{-4}$ of the total generated neutrons interact with the fiducial volume in the energy region of interest, while $P_2 = 1.982 \times 10^{-5}$ of the total generated neutrons interact with the highest energy bin in the region of interest—ranging from 23 keVee to 25 keVee. Values for P_1 and P_2 are summarized in table 4.1.

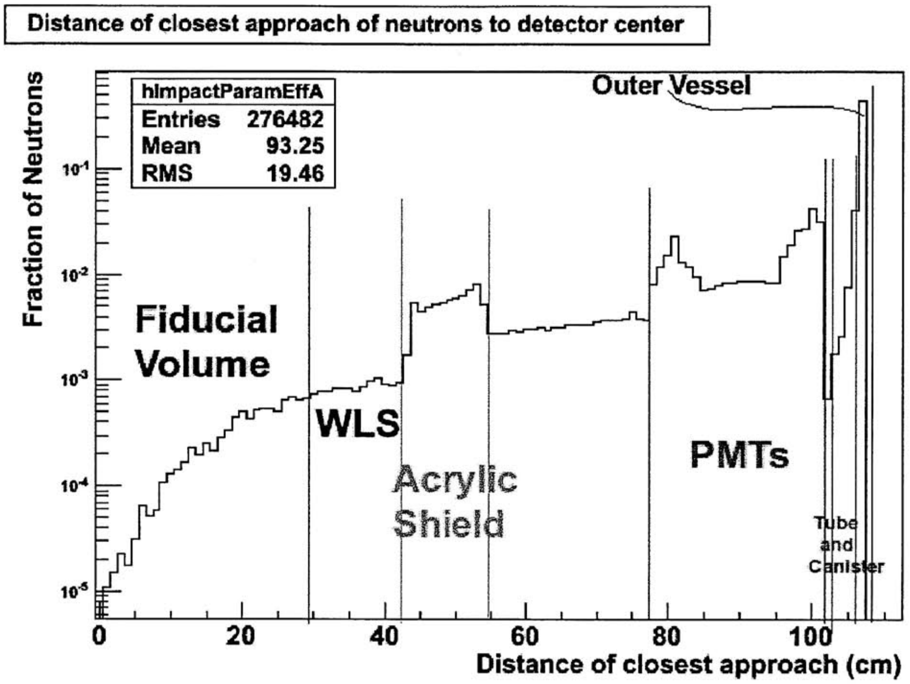

Figure 4-12: The spatial distribution of neutron interactions as they passed from the d-d source to the center of the detector. The histogram bins how many interactions occurred at each radius for the full calibration geometry. Features on the histogram are labeled with which parts of the detector they occur at, including the outer vessel wall, the tube and canister, the photomultiplier tubes, the acrylic shields, the wavelength shifter, and the fiducial volume. Note that the unlabeled regions between the photomultiplier tubes and fiducial volume are all filled with liquid argon.

Calculating the required number of neutrons for 5% statistical errors as we did

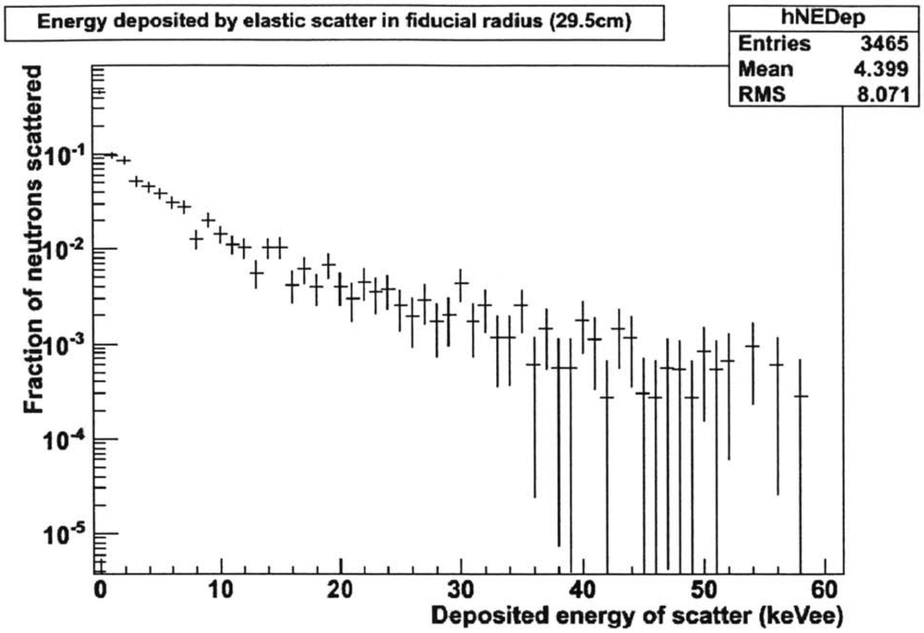

Figure 4-13: The normalized deposited energy distribution from neutron interactions within the fiducial volume for the full calibration geometry

above, we obtain the final calibration requirements shown in table 4.2. Here, we see that adding the rest of the canister had little effect on the neutron interactions within the region of interest. Adding the calibration tube caused a decrease in the neutron spectrum by approximately a factor of 10, while adding the canister only caused a decrease of approximately 20%.

Since we are producing approximately 10^5 neutrons per second and each pulse will produce neutrons for 1 μs, we expect an average of 0.1 neutrons to be produced per pulse. Since we observed 3465 neutron interactions within the fiducial volume out of the 9×10^5 neutrons that were produced, we find that 3.85×10^{-3} of the neutrons produced will interact within the fiducial radius and that there will be 3.85×10^{-4} neutron interactions within the fiducial radius per pulse. This means that the neutron events will be sufficiently spaced apart that they will not interact too quickly to be read by the 10 μs DAQ readout window.

Geometry	P_1	P_2
Standard	2.62×10^{-4}	3.53×10^{-5}
With Tube	1.93×10^{-4}	1.94×10^{-5}
Full	1.611×10^{-4}	1.982×10^{-5}

Table 4.1: The proportion of simulated neutron interactions within the region of interest in the fiducial volume (P_1) and the proportion of simulated neutron interactions within the highest bin of the region of interest in the fiducial volume (P_2).

Geometry		Neutrons Needed	On Time (s)	Total Time (s)
Standard	Energy Spectrum	1.53×10^6	15.3	76.5
	Counting	1.13×10^7	113	565
With Tube	Energy Spectrum	2.07×10^6	20.7	104
	Counting	2.06×10^7	206	1030
Full	Energy Spectrum	2.48×10^6	24.8	124
	Counting	2.02×10^7	201	1005

Table 4.2: The number of neutrons that need to be produced to reach 5% counting and energy spectrum measurements and the total amount of time the d-d source must be on in order to reach this precision, assuming neutrons are produced at a rate of 10^5 neutrons per second

Chapter 5

Conclusions

We have successfully designed a prototype deployment system for the calibration neutron source for the MiniCLEAN dark matter detector. This system includes electronics and software to deploy the source, a canister to hold the neutron source, a computer-controlled winch and yo-yo potentiometer feedback system to lower the neutron source to a specified location, and a cable arrangement to supply power and structural support to the neutron source and canister so that the neutron source can be pulsed during the calibration.

We have tested the deployment system and found that it is precise to approximately 0.05 cm, well within our target precision of 0.5 cm. We have designed a prototype for the canister in AutoCAD and found that the deployment system maintained its precision when lowering a weighted canister from a realistic height of 8 feet.

We also calculated the heat load of the calibration neutron source on the surrounding dielectric gel. We found that the temperature of the gel will increase by $92.6^{+56.8}_{-18.8}$ K due to this head load. This temperature increase is within the service temperature range of the gel, as specified in Appendix D. This temperature increase will cause the gel to expand in volume by $35.3^{+22.7}_{-7.4}$ mL. We recommend that between 1.18 cm and 2.46 cm be left between the top of the gel and the top cap of the canister for clearance as the gel expands. More precise knowledge of the thermal conductivity of the dielectric gel will decrease our uncertainty on these numbers. The temperature rise is within the service temperature of the dielectric gel.

We simulated the external neutron background in MiniCLEAN and found that the addition of an air-filled calibration tube has little effect on the total external neutron background rate within the fiducial volume and energy region of interest.

We simulated MiniCLEAN's calibration process and found that the number of neutron-nucleus recoils within the fiducial volume of the detector in the energy region of interest is increased by a factor of two by the addition of the calibration tube, but is changed very little by the addition of the canister, dielectric gel, and acrylic holder. We also found that the canister and tube geometry have little effect on the overall calibration neutron-induced recoil energy spectrum, as can be seen in figure 5-1.

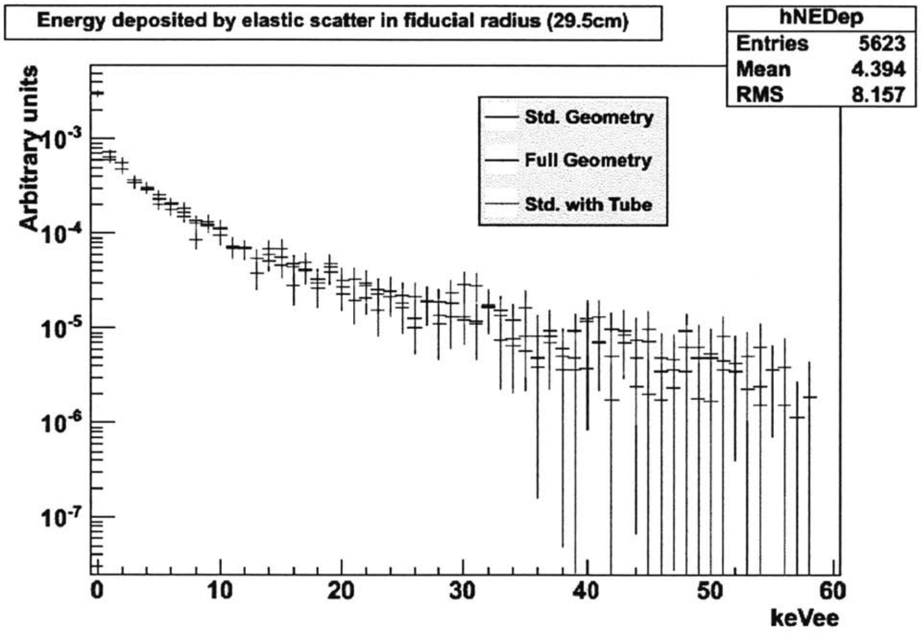

Figure 5-1: The energy spectra for neutron-induced recoils within the fiducial volume for the standard geometry, the full calibration geometry, and the standard geometry with an added calibration tube. All three spectra are within error of each other, showing that the geometries had little effect on the neutron-induced recoil energy spectrum.

Our simulations show that in order to integrate sufficient statistics to achieve a 5% measurement of the calibration neutron-induced recoil spectrum, we will need to run the neutron source in pulse mode for at least 1005 seconds. We recommend that the neutron source is run for this long once per day in order to calibrate the dark matter detector response to nuclear recoils, while maintaining low dead time.

Appendix A

High Voltage Feedthrough Technical Data

GES High Voltage Feedthrough SB 150, from [12]

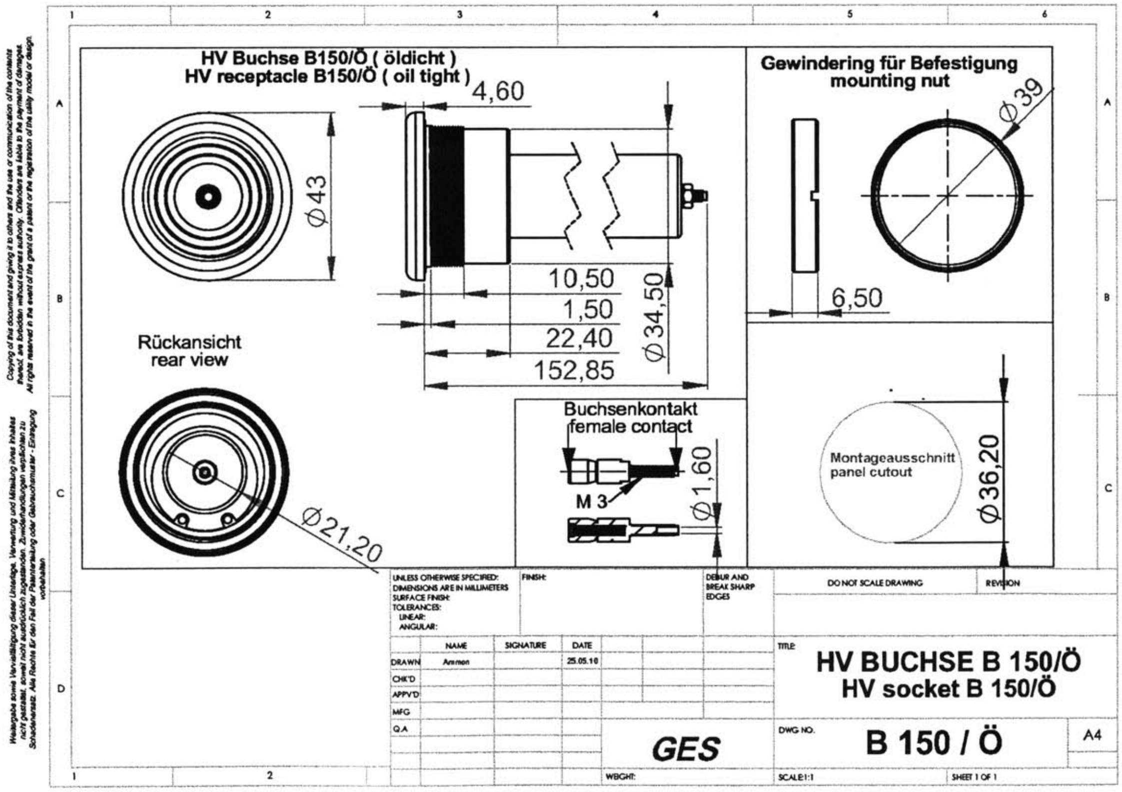

Appendix B

PAVE Feedthrough Technical Data

PAVE Seal Cable Harness feedthrough[7].

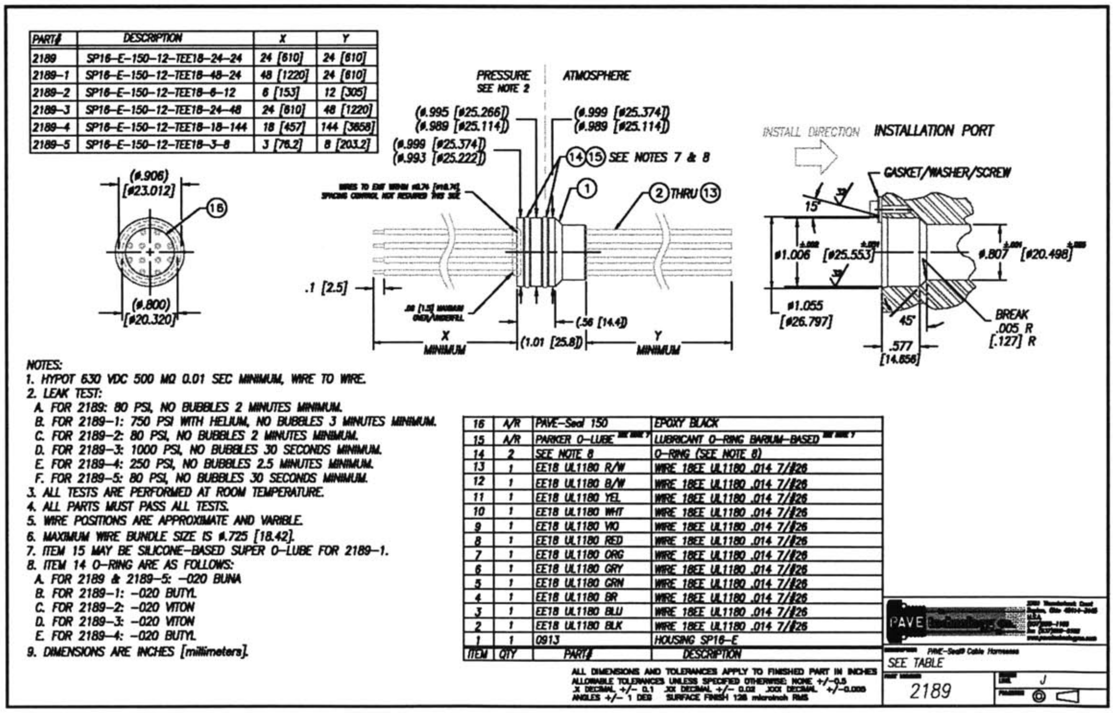

PART#	DESCRIPTION	X	Y
2189	SP16-E-150-12-TEE18-24-24	24 [610]	24 [610]
2189-1	SP16-E-150-12-TEE18-48-24	48 [1220]	24 [610]
2189-2	SP16-E-150-12-TEE18-6-12	6 [153]	12 [305]
2189-3	SP16-E-150-12-TEE18-24-48	24 [610]	48 [1220]
2189-4	SP16-E-150-12-TEE18-18-144	18 [457]	144 [3658]
2189-5	SP16-E-150-12-TEE18-3-8	3 [76.2]	8 [203.2]

NOTES:
1. HYPOT 630 VDC 500 MΩ 0.01 SEC MINIMUM, WIRE TO WIRE.
2. LEAK TEST:
   A. FOR 2189: 80 PSI, NO BUBBLES 2 MINUTES MINIMUM.
   B. FOR 2189-1: 750 PSI WITH HELIUM, NO BUBBLES 3 MINUTES MINIMUM.
   C. FOR 2189-2: 80 PSI, NO BUBBLES 2 MINUTES MINIMUM.
   D. FOR 2189-3: 1000 PSI, NO BUBBLES 30 SECONDS MINIMUM.
   E. FOR 2189-4: 250 PSI, NO BUBBLES 2.5 MINUTES MINIMUM.
   F. FOR 2189-5: 80 PSI, NO BUBBLES 30 SECONDS MINIMUM.
3. ALL TESTS ARE PERFORMED AT ROOM TEMPERATURE.
4. ALL PARTS MUST PASS ALL TESTS.
5. WIRE POSITIONS ARE APPROXIMATE AND VARIBLE.
6. MAXIMUM WIRE BUNDLE SIZE IS ø.725 [18.42].
7. ITEM 15 MAY BE SILICONE-BASED SUPER O-LUBE FOR 2189-1.
8. ITEM 14 O-RING ARE AS FOLLOWS:
   A. FOR 2189 & 2189-5: -020 BUNA
   B. FOR 2189-1: -020 BUTYL
   C. FOR 2189-2: -020 VITON
   D. FOR 2189-3: -020 VITON
   E. FOR 2189-4: -020 BUTYL
9. DIMENSIONS ARE INCHES [millimeters].

ITEM	QTY	PART#	DESCRIPTION
16	A/R	PAVE-Seal 150	EPOXY BLACK
15	A/R	PARKER O-LUBE	LUBRICANT O-RING BARIUM-BASED
14	2	SEE NOTE 8	O-RING (SEE NOTE 8)
13	1	EE18 UL1180 R/W	WIRE 18EE UL1180 .014 7/#26
12	1	EE18 UL1180 B/W	WIRE 18EE UL1180 .014 7/#26
11	1	EE18 UL1180 YEL	WIRE 18EE UL1180 .014 7/#26
10	1	EE18 UL1180 WHT	WIRE 18EE UL1180 .014 7/#26
9	1	EE18 UL1180 VIO	WIRE 18EE UL1180 .014 7/#26
8	1	EE18 UL1180 RED	WIRE 18EE UL1180 .014 7/#26
7	1	EE18 UL1180 ORG	WIRE 18EE UL1180 .014 7/#26
6	1	EE18 UL1180 GRY	WIRE 18EE UL1180 .014 7/#26
5	1	EE18 UL1180 GRN	WIRE 18EE UL1180 .014 7/#26
4	1	EE18 UL1180 BR	WIRE 18EE UL1180 .014 7/#26
3	1	EE18 UL1180 BLU	WIRE 18EE UL1180 .014 7/#26
2	1	EE18 UL1180 BLK	WIRE 18EE UL1180 .014 7/#26
1	1	0913	HOUSING SP16-E

ALL DIMENSIONS AND TOLERANCES APPLY TO FINISHED PART IN INCHES
ALLOWABLE TOLERANCES UNLESS SPECIFIED OTHERWISE: NONE +/-0.5
.X DECIMAL +/- 0.1 .XX DECIMAL +/- 0.02 .XXX DECIMAL +/-0.005
ANGLES +/- 1 DEG SURFACE FINISH 125 microinch RMS

Appendix C

High Voltage Source Technical Data

Model: Spellman SL30, from [10]

Specification	Value
Input Voltage	115 V_{AC}
Output Voltage	30 kV
Ripple	0.1% p-p of maximum output
Temperature Coefficient	100 ppm/°C voltage
Operating Temperature	0°C to 50°C
Storage Temperature	-40°C to 85°C
Stability after 1/2 hour warm-up	100 ppm/hour
Output Cable Length	10 feet (shielded)
Input Cable Length	6 feet
Height	1.75 inches
Width×Depth	19 inches × 19 inches
Weight	17 lbs

Appendix D

Dielectric Gel Technical Data

Dow Corning 5 Compound

Physical Properties[9]

Property	Value
Color	Translucent light gray
Penetration (unworked)	200
Penetration (worked, 60 strokes maximum)	210
Bleed (24 hours/200°C)	3.5%
Evaporation (24 hours/200°C)	1%
Service Temperature Range	-54°C to 232°C
Specific Gravity at 25°C	1.0
Coefficient of Thermal Expansion[8]	$7\times10^{-4}\mathrm{K}^{-1}$
Thermal Conductivity[32]	$0.25\pm0.13\ \mathrm{Wm}^{-1}\mathrm{K}^{-1}$

Electric Properties[9]

Property	Value
Dielectric Constant @ 100 Hz	2.99
Dielectric Constant @ 100 kHz	2.94
Dissipation Factor @ 100 Hz	< 0.0003
Dissipation Factor @ 100 kHz	< 0.0001
Dielectric Strength (50-mil gap)	545 volts/mil
Volume Resistivity @ 23°C	1.1×10^{15} ohm-cm
Arc Resistance	101 s

Appendix E

USB DAC Technical Data

Model: LabJack U3-HV[36]

- 12 Flexible I/O Inputs
- 4 Dedicated HV Analog Inputs with ±10 V or -10/+20 V Range
- 4 Additional Digital I/O Inputs
- 2 Analog Ouputs
- Supports SPI, I2C, and Asynchronous Serial Protocols (Master Only)
- Supports Software or Hardware Timed Acquisition
- Maximum Input Stream Rate of 2.5-50 kHz (Depending on Resolution)
- Capable of Command/Response Times Less Than 1 Millisecond
- Built-In Screw Terminals for Some Signals
- USB 2.0/1.1 Full Speed Interface
- Powered by USB Cable
- Drivers Available for Windows, Linux, Mac and Pocket PC
- 12 LV Inputs (Flexible I/O)

Appendix F

Yoyo Potentiometer Technical Data

Celesco Cable-Extension Position Transducer, from [6].

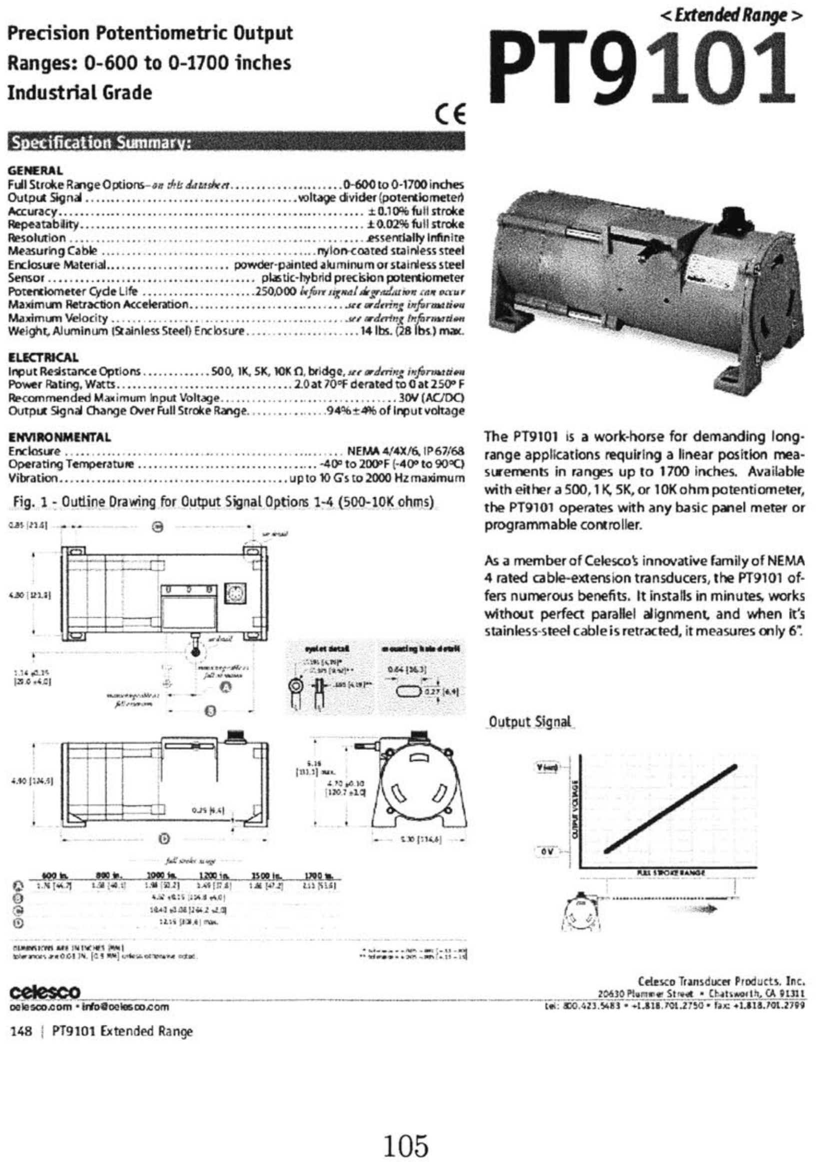

Precision Potentiometric Output
Ranges: 0-600 to 0-1700 inches
Industrial Grade

< Extended Range >

PT9101

Specification Summary:

GENERAL

Full Stroke Range Options–*on this datasheet*	0-600 to 0-1700 inches
Output Signal	voltage divider (potentiometer)
Accuracy	±0.10% full stroke
Repeatability	±0.02% full stroke
Resolution	essentially infinite
Measuring Cable	nylon-coated stainless steel
Enclosure Material	powder-painted aluminum or stainless steel
Sensor	plastic-hybrid precision potentiometer
Potentiometer Cycle Life	250,000 *before signal degradation can occur*
Maximum Retraction Acceleration	*see ordering information*
Maximum Velocity	*see ordering information*
Weight, Aluminum (Stainless Steel) Enclosure	14 lbs. (28 lbs.) max.

ELECTRICAL

Input Resistance Options	500, 1K, 5K, 10K Ω, bridge, *see ordering information*
Power Rating, Watts	2.0 at 70°F derated to 0 at 250° F
Recommended Maximum Input Voltage	30V (AC/DC)
Output Signal Change Over Full Stroke Range	94% ± 4% of input voltage

ENVIRONMENTAL

Enclosure	NEMA 4/4X/6, IP 67/68
Operating Temperature	-40° to 200°F (-40° to 90°C)
Vibration	up to 10 G's to 2000 Hz maximum

Fig. 1 - Outline Drawing for Output Signal Options 1-4 (500-10K ohms)

The PT9101 is a work-horse for demanding long-range applications requiring a linear position measurements in ranges up to 1700 inches. Available with either a 500, 1K, 5K, or 10K ohm potentiometer, the PT9101 operates with any basic panel meter or programmable controller.

As a member of Celesco's innovative family of NEMA 4 rated cable-extension transducers, the PT9101 offers numerous benefits. It installs in minutes, works without perfect parallel alignment, and when it's stainless-steel cable is retracted, it measures only 6".

Output Signal

celesco
celesco.com • info@celesco.com

Celesco Transducer Products, Inc.
20630 Plummer Street • Chatsworth, CA 91311
tel: 800.423.5483 • +1.818.701.2750 • fax: +1.818.701.2799

148 | PT9101 Extended Range

Ordering Information:

Model Number:

PT9101- ____ Ⓡ - __ Ⓐ **1** Ⓑ __ Ⓒ - __ Ⓓ **1** Ⓔ __ Ⓕ **0** Ⓖ
order code:

Sample Model Number:

PT9101 - 1200 - 111 - 1110

Ⓡ range:	1200 inches
Ⓐ enclosure:	aluminum
Ⓒ cable exit:	front
Ⓓ output signal:	500 ohm potentiometer
Ⓕ electrical connection:	6-pin plastic connector

Full Stroke Range:

Ⓡ *order code:*	0600	0800	1000	1200	1500	1700
full stroke range, min:	600 in.	800 in.	1000 in.	1200 in.	1500 in.	1700 in.
cable tension (30%):	25 oz.	25 oz.	24 oz.	24 oz.	23 oz.	23 oz.
measuring cable:	.034-in. dia. nylon-coated stainless	.019-in. dia. nylon-coated stainless	.019-in. dia. nylon-coated stainless	.019-in. dia. nylon-coated stainless	.014-in. dia. nylon-coated stainless	.014-in. dia. nylon-coated stainless

Enclosure Material:

Ⓐ *order code:*	1	3
enclosure material:	powder-painted aluminum	303 stainless steel
max. acceleration:	1G	.33G
max. velocity:	60 inches/sec.	20 inches/sec.

Cable Exit:

Ⓒ *order code:*	1	2	3	4
	front	top	back	down
	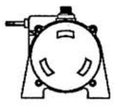	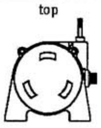	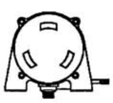	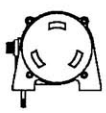

Output Signals:

Ⓓ *order code:*	1	2	3	4	5	6
	500 ohm*	1000 ohm*	5000 ohm*	10,000 ohm*	fixed bridge (2 mV/V)	adjustable bridge (0...30 mV/V)

**tolerance = ±10%*

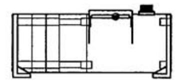

enclosure outline drawing
see fig 1.

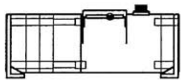

enclosure outline drawing
see fig 2.

circuit, options 1-4

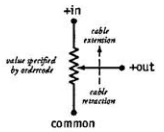

fixed bridge circuit

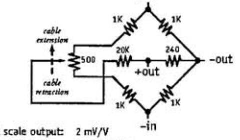

full scale output: 2 mV/V
zero adjust: not available

adjustable bridge cicuit

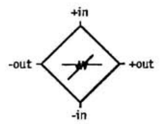

full scale output: adjustable from 0 to 30mV/V
zero adjust: from factory set zero to 50% of full stroke

Appendix G

Winch Control Functions

The following functions interface with the U3 LabJack USB DAC (see Appendix E for technical specifications on this device) to control the winch to raise and lower the canister position.

To set the winch to raise and lower the canister when turned on, use the following two functions:

```
/// Function to set the motor to move up ///
/* ------------------------------------------------------------
   input: none
   output: 0 if success, else error
   Note: This will tell the motor to move up, but the motor
         will not actually move up until it is turned on
   ------------------------------------------------------------ */
long set_motor_up()
{
  HANDLE hDevice;
  int localID;
  long error;
  u3CalibrationInfo caliInfo;
```

```
  // Open first found U3 over USB
  localID = -1;
  if( (hDevice = openUSBConnection(localID)) == NULL)
    goto done;

  // Set the motor to go up
  if((error = eDAC(hDevice, &caliInfo, 0, 1, 5., 0, 0, 0)) != 0)
    goto close;

 close:
  if(error > 0)
    printf(”Received␣an␣error␣code␣of␣%ld\n”,error);
  closeUSBConnection(hDevice);
 done:
  return error;
}

/// Function to set the motor to move down ///
/* ------------------------------------------------------------
   input: none
   output: 0 if success, else error
   Note: This will tell the motor to move up, but the motor
         will not actually move up until it is turned on
   ------------------------------------------------------------ */
long set_motor_down()
{
  HANDLE hDevice;
  int localID;
  long error;
  u3CalibrationInfo caliInfo;
```

```
  // Open first found U3 over USB
  localID = -1;
  if( (hDevice = openUSBConnection(localID)) == NULL)
    goto done;

  // Set the motor to go down
  if((error = eDAC(hDevice, &caliInfo , 0, 1, 0., 0, 0, 0)) != 0)
    goto close;

 close:
  if(error > 0)
    printf("Received␣an␣error␣code␣of␣%ld\n",error);
  closeUSBConnection(hDevice);
 done:
  return error;
}
```

To turn the power to the winch on and off use the following two functions:

```
/// Function to set the motor power on ///
/* ------------------------------------
   input: none
   output: 0 if success, else error
   ------------------------------------ */
long set_motor_on()
{
  HANDLE hDevice;
  int localID;
  long error;
  u3CalibrationInfo caliInfo;
```

```
  // Open first found U3 over USB
  localID = -1;
  if( (hDevice = openUSBConnection(localID)) == NULL)
    goto done;

  // Set the motor power on
  if((error = eDAC(hDevice, &caliInfo, 0, 0, 1., 0, 0, 0)) != 0)
    goto close;

 close:
  if(error > 0)
    printf("Received␣an␣error␣code␣of␣%ld\n",error);
  closeUSBConnection(hDevice);
 done:
  return error;
}

/// Function to set the motor power off ///
/* ------------------------------------------
   input: none
   output: 0 if success, else error
   ------------------------------------------ */
long set_motor_off()
{
  HANDLE hDevice;
  int localID;
  long error;
  u3CalibrationInfo caliInfo;
```

```
  // Open first found U3 over USB
  localID = -1;
  if( (hDevice = openUSBConnection(localID)) == NULL)
    goto done;

  // Set the motor power off
  if((error = eDAC(hDevice, &caliInfo, 0, 0, 0., 0, 0, 0)) != 0)
    goto close;

 close:
  if(error > 0)
    printf("Received an error code of %ld\n",error);
  closeUSBConnection(hDevice);
 done:
  return error;
}
```

Bibliography

[1] R. Adams. Method of continuously casting steel. Patent, October 1964.

[2] N. Franco B. Buck. Neutron source power supplies: Design and construction of power supplies for a neutron source to calibrate dark matter experiments. Master's project, Worcester Polytechnic Institute, Physics Department, 2009.

[3] K. Begeman. H I rotation curves of spiral galaxies. I - NGC 3198. *Astronomy and Astrophysics*, 223(1–2):47–60, 1989.

[4] M. Boulay and A. Hime. Technique for direct detection of weakly interacting massive particles using scintillation time discrimination in liquid argon. *Astroparticle Physics*, 25(3):179–182, 2006.

[5] C. Conroy, R. Wechsler, and A. Kravtsov. Modeling Luminosity-Dependent Galaxy Clustering Through Cosmic Time. *Astrophys. J.*, 647:201–214, 2006.

[6] Celesco. Pt9101 cable-extension position transducer product data sheet. Technical data sheet. Found at http://celesco.com/_datasheets/pt9101.pdf.

[7] PAVE Technology Co. Pave seal cable harness. Technical data sheet. Found at http://www.pavetechnologyco.com/design/pdf/2189.html.

[8] RS Components. *Technical Data Sheet: General Purpose Silicone Grease.* RS Components, PO Box 99, Corby NN 17 9RS, 810.1 edition, 2011.

[9] Dow Corning 5 Compound. *Product Information: Specialty Lubricants.* Dow Corning, agp4934 edition, 1996.

[10] Spellman High Voltage Electronics Corporation. Sl series high voltage supply instruction manual. Technical data sheet. Found at http://www.spellmanhv.com/en/Technical-Resources/~/media/Files/Technical-Resources/Manuals/SLMAN.ashx.

[11] W. de Blok and S. McGaugh. The dark and baryonic matter content of low surface brightness disk galaxies. *Mon. Not. Roy. Astron. Soc.*, 290:533–552, 1997.

[12] GES Electronic and Service. Hv busche b 150. Technical data sheet, May 2010. Found at http://www.ges-electronic.com/connector/singlepin_hv_ser_100_sb_150.php.

[13] A. Wagner et al. A Search for Hidden Sector Photons with ADMX. *Phys. Rev. Lett.*, 105:171801, 2010.

[14] D. Clowe et al. A direct empirical proof of the existence of dark matter. *Astrophys. J.*, 648:L109–L113, 2006.

[15] D. Mei et. al. Evaluation of (alpha,n) Induced Neutrons as a Background for Dark Matter Experiments. *Nucl. Instrum. Meth.*, A606:651–660, 2009.

[16] E. Aprile et al. Dark Matter Results from 100 Live Days of XENON100 Data. 2011.

[17] G. Cassiday et al. Calculation of the stopping-muon rate underground. *Phys. Rev. D*, 7(7):2022–2031, Apr 1973.

[18] G. Hinshaw et al. Five-Year Wilkinson Microwave Anisotropy Probe (WMAP 1) Observations:Data Processing, Sky Maps, & Basic Results. *Astrophys. J. Suppl.*, 180:225–245, 2009.

[19] J. Angle et al. First Results from the XENON10 Dark Matter Experiment at the Gran Sasso National Laboratory. *Phys. Rev. Lett.*, 100:021303, 2008.

[20] J. Battat et al. DMTPC: A dark matter detector with directional sensitivity. *AIP Conf. Proc.*, 1182:276–279, 2009.

[21] L. Wyrzykowski et al. The OGLE View of Microlensing towards the Magellanic Clouds. III. Ruling out sub-solar MACHOs with the OGLE-III LMC data. 2010.

[22] R. Bernabei et al. First results from DAMA/LIBRA and the combined results with DAMA/NaI. *Eur. Phys. J.*, C56:333–355, 2008.

[23] R. Bernabei et al. The DAMA/LIBRA apparatus. *Nucl. Instrum. Meth.*, A592:297–315, 2008.

[24] V. Gehman et al. Fluorescence Efficiency and Visible Re-emission Spectrum of Tetraphenyl Butadiene Films at Extreme Ultraviolet Wavelengths. 2011.

[25] W. Lippincott et al. Calibration of liquid argon and neon detectors with $^{83}Kr^m$. *Phys. Rev.*, C81:045803, 2010.

[26] Z. Ahmed et al. Results from a Low-Energy Analysis of the CDMS II Germanium Data. 2010.

[27] L. Feng. Miniclean neutron calibration system. Technical note on MiniCLEAN calibration hardarware, 2010.

[28] G. Jungman, M. Kamiokowski, and K. Griest. Supersymmetric dark matter. *Physics Reports*, 267:195–373, 1996.

[29] *Handbook of Compressed Gases*, 4 Ed, Editor Kluwer Academic Pub, 1999.

[30] Arkema Group. *Typical Physical Properties, Acrylic Resin.* Altuglas International, 2000 Market Street, Philadelphia, PA 19103, 2006.

[31] E. Hercus and D. Sutherland. Thermal Conductivity of Air by Parallel Plate Method. *Proceedings of the Royal Society of London. Series A, Containing Papers of a Mathematical and Physical Character*, 145(855):599–611, 1934.

[32] P. Houck. e-mail correspondence regarding the corning 5 compound dielectric gel silicone grease.

[33] M Maltoni J. Kopp and T. Schwetz. Are there sterile neutrinos at the eV scale? 2011.

[34] G. Fuller K. Abazajian and M. Patel. Sterile neutrino hot, warm, and cold dark matter. *Phys. Rev. D*, 64(2):023501, May 2001.

[35] B. Fields K. Freese and D. Graff. Limits on Stellar Objects as the Dark Matter of Our Halo: Nonbaryonic Dark Matter Seems to be Required. 1999.

[36] LabJack. *U3 LabJack Specifications.* LabJack Corporation, 3232 S Vance St STE 100, Lakewood, CO 80227 USA, 2011. Data sheet from <http://labjack.com/u3/specs>.

[37] J. Lewin and P. Smith. Review of mathematics, numerical factors, and corrections for dark matter experiments based on elastic nuclear recoil. *Astroparticle Physics*, 6(1):87–112, 1996.

[38] M. Markevitch. Constraints on physics of gas and dark matter from cluster mergers. Talk given in Nov. 2005, found at http://cxc.harvard.edu/symposium_2005/proceedings/files/markevitch_maxim.pdf.

[39] D. Mei and A. Hime. Muon-Induced Background Study for Underground Laboratories. *Phys. Rev.*, D73:053004, 2006.

[40] M. Moniez. Review of results from EROS Microlensing search for Massive Compact Objects. 2009.

[41] R. Peccei and H. Quinn. *cp* conservation in the presence of pseudoparticles. *Phys. Rev. Lett.*, 38(25):1440–1443, Jun 1977.

[42] A. Incicchitti R. Bernabei, P. Belli and D. Prosperi. Liquid Noble gases for Dark Matter searches: a synoptic survey. 2008.

[43] T. Agekyan, I. Petrovskaya, and B. Fresenko. Galactic Rotation from Radio Observations. *Soviet Astronomy-AJ*, 41:1027–L1037, 2006.

[44] M. Kuzniak T. Pollmann, M. Boulay. Scintillation of thin tetraphenyl butadiene films under alpha particle excitation. 2010.

[45] et al. W. Lippincott. Scintillation time dependence and pulse shape discrimination in liquid argon. *Phys. Rev. C*, 78(3):035801, Sep 2008.

[46] NASA WMAP. Content of the universe pie chart. http://map.gsfc.nasa.gov/media/080998/index.html.